



HAL
open science

Highly efficient 2.3 μm thulium lasers based on a high-phonon-energy crystal: Evidence of vibronic-assisted emissions

Pavel Loiko, Esrom Kifle, Lauren Guillemot, Jean-Louis Doualan, Florent Starecki, A. Braud, Magdalena Aguiló, Francesc Díaz, Valentin Petrov, Xavier Mateos, et al.

► To cite this version:

Pavel Loiko, Esrom Kifle, Lauren Guillemot, Jean-Louis Doualan, Florent Starecki, et al.. Highly efficient 2.3 μm thulium lasers based on a high-phonon-energy crystal: Evidence of vibronic-assisted emissions. *Journal of the Optical Society of America B*, 2021, 38 (2), pp.482. 10.1364/JOSAB.411075 . hal-03140560

HAL Id: hal-03140560

<https://hal.science/hal-03140560v1>

Submitted on 7 Oct 2021

HAL is a multi-disciplinary open access archive for the deposit and dissemination of scientific research documents, whether they are published or not. The documents may come from teaching and research institutions in France or abroad, or from public or private research centers.

L'archive ouverte pluridisciplinaire **HAL**, est destinée au dépôt et à la diffusion de documents scientifiques de niveau recherche, publiés ou non, émanant des établissements d'enseignement et de recherche français ou étrangers, des laboratoires publics ou privés.

Queries

1. AU: Are changes to the title okay?
2. AU: References must be cited in order in the text. We have renumbered the references to achieve this. Please check carefully the citations in text that they are accurate and in order.
3. AU: We closed up the spacing around the dash in "m-1-phonon" in the sentence beginning "C has the meaning of a NR rate constant in the limit. . ." Please check.
4. AU: The funding information for this article has been generated using the information you provided to OSA at the time of article submission. Please check it carefully. If any information needs to be corrected or added, please provide the full name of the funding organization/institution as provided in the CrossRef Open Funder Registry (<https://search.crossref.org/funding>).

Highly efficient 2.3 μm thulium lasers based on a high-phonon-energy crystal: evidence of vibronic-assisted emissions

PAVEL LOIKO,¹ ESROM KIFLE,¹ LAUREN GUILLEMOT,¹  JEAN-LOUIS DOUALAN,¹
FLORENT STARECKI,¹ ALAIN BRAUD,¹ MAGDALENA AGUILÓ,² FRANCESC DÍAZ,²
VALENTIN PETROV,³ XAVIER MATEOS,²  AND PATRICE CAMY^{1,*}

¹Centre de Recherche sur les Ions, les Matériaux et la Photonique (CIMAP), UMR 6252 CEA-CNRS-ENSICAEN, Université de Caen Normandie, 6 Boulevard du Maréchal Juin, 14050 Caen Cedex 4, France

²Universitat Rovira i Virgili (URV), Física i Cristal·lografia de Materials i Nanomaterials (FiCMA-FiCNA)-EMaS, Marcel·li Domingo 1, 43007 Tarragona, Spain

³Max Born Institute for Nonlinear Optics and Short-Pulse Spectroscopy, 2A Max-Born-Str., 12489 Berlin, Germany

*Corresponding author: patrice.camy@ensicaen.fr

Received 24 September 2020; revised 9 December 2020; accepted 12 December 2020; posted 15 December 2020 (Doc. ID 411075); published 0 MONTH 0000

1 We report on highly efficient and power-scalable laser operation in a thulium-doped high-phonon-energy crystal [monoclinic double tungstate, $\text{KLu}(\text{WO}_4)_2$] on the ${}^3\text{H}_4 \rightarrow {}^3\text{H}_5$ Tm^{3+} transition giving rise to the short-wave infrared emission at $\sim 2.3 \mu\text{m}$. A 3 at. % Tm -doped crystal generated a maximum continuous-wave output power of 1.12 W at ~ 2.22 and $2.29 \mu\text{m}$ with a record-high slope efficiency of 69.2% (versus the absorbed pump power), a slightly multimode beam ($M_{x,y}^2 = 2.2$ and 2.6), and a linear laser polarization. The $\sim 2.3 \mu\text{m}$ laser outperformed the one operating on the conventional ${}^3\text{F}_4 \rightarrow {}^3\text{H}_6$ transition (at $\sim 1.95 \mu\text{m}$). The effect of the Tm concentration on the $\sim 2.3 \mu\text{m}$ laser performance indicates a gradually increasing pump quantum efficiency for the ${}^3\text{H}_4$ upper laser level with the Tm doping. For the 3 at. % Tm -doped crystal, it reached 1.8 ± 0.1 (almost two-for-one pump process), which is attributed to efficient energy-transfer upconversion. We discuss the physical nature of the laser emissions occurring at intermediate wavelengths between the electronic ${}^3\text{H}_4 \rightarrow {}^3\text{H}_5$ and ${}^3\text{F}_4 \rightarrow {}^3\text{H}_6$ transitions and highlight the role of electron-phonon coupling (vibronic processes) in the appearance of such laser lines. This allowed us to better understand the near- and mid-infrared emission from thulium ions, which can be used in broadly tunable and fs mode-locked 2–2.3 μm lasers. © 2020 Optical Society of America

<https://doi.org/10.1364/JOSAB.411075>

1. INTRODUCTION

2 In recent years, coherent light sources emitting near 2.3 μm in the short-wavelength infrared (SWIR) spectral range have attracted increasing attention. Such emission falls into the atmosphere transparency window with weak water vapor absorption containing at the same time absorption lines of atmospheric pollutants, i.e., hydrogen fluoride (HF), carbon monoxide (CO), methane (CH_4), or formaldehyde (H_2CO). Consequently, $\sim 2.3 \mu\text{m}$ lasers find applications in gas sensing in the atmosphere [1,2] and optical metrology of combustion processes [3]. They are also promising for non-invasive glucose ($\text{C}_6\text{H}_{12}\text{O}_6$) blood measurements [4]. Potentially, ultrafast $\sim 2.3 \mu\text{m}$ lasers can be used for further frequency conversion into the mid-IR [5].

There exist several possibilities to obtain emission near 2.3 μm from solid-state lasers. Cr^{2+} -doped II–IV group materials—zinc chalcogenides (ZnS , ZnSe)—give rise to a

broadly tunable laser emission covering the desired wavelength [6]. Sorokina *et al.* reported on a continuous-wave (CW) $\text{Cr}^{2+}:\text{ZnS}$ laser delivering 100 mW at $\sim 2.35 \mu\text{m}$ with a slope efficiency of 16%, tunable between 2.19 and $2.47 \mu\text{m}$ [7]. Further power scaling reaching multi-watt regime at improved slope efficiency was demonstrated later on [6,8]. Mode-locked (ML) $\text{Cr}^{2+}:\text{ZnS}$ and $\text{Cr}^{2+}:\text{ZnSe}$ lasers generating femtosecond (fs) pulses are also known [9,10]. However, the fabrication of high-optical quality zinc chalcogenide crystals and ceramics is complex. Moreover, such lasers require special pump sources, such as Co^{2+} lasers at $\sim 1.67 \mu\text{m}$ or Tm^{3+} fiber or bulk lasers at $\sim 1.9 \mu\text{m}$.

Another possibility is the use of semiconductor structures (GaInAs on InP or GaInAsSb on GaSb), e.g., in diode lasers [11] or vertical-cavity surface-emitting lasers (VECSELs) [12]. Besides the relatively complex design and fabrication methods, the power scaling capabilities of such lasers (single-emitters)

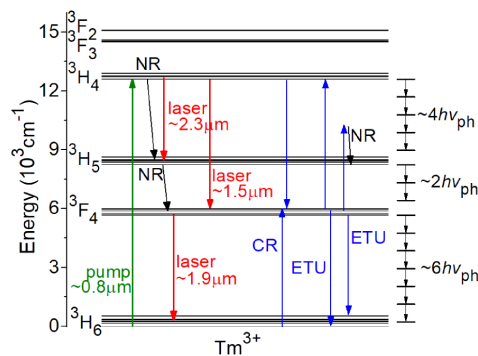


Fig. 1. Energy level scheme of the Tm^{3+} ion in the high-phonon-energy monoclinic double tungstate crystal $\text{KLu}(\text{WO}_4)_2$ (after [14]), showing the pump transition (green arrow), laser transitions (red arrows), cross-relaxation (CR), and energy-transfer upconversion (ETU). NR is the non-radiative decay. The equally separated horizontal dashes show the average number of high-energy phonons ($h\nu_{ph}$) needed to bridge the energy-gaps between the multiplets involved in laser emission.

are limited. Geerlings *et al.* presented a GaSb-based diode laser generating 16.5 mW at $\sim 2.23 \mu\text{m}$ with a wavelength tunability between 2.21 and 2.39 μm [11]. The output power can be scaled reaching watt-level in array configuration, however, with a trade-off on spatial quality [13]. In addition, the ultrafast operation of such lasers has been poorly studied.

Finally, $\sim 2.3 \mu\text{m}$ emission can be obtained using thulium (Tm^{3+})-doped materials based on the ${}^3\text{H}_4 \rightarrow {}^3\text{H}_5$ quasi-four-level transition, Fig. 1(a). This laser scheme has been long known both for bulk [15] and fiber [16] lasers. However, it was considered to be inefficient, and the ${}^3\text{F}_4 \rightarrow {}^3\text{H}_6$ transition at $\sim 2 \mu\text{m}$ received much more attention [17]. At a glance, there are several difficulties in realizing $\sim 2.3 \mu\text{m}$ Tm lasers, i.e., (i) relatively short radiative lifetime of the upper laser level (${}^3\text{H}_4$) and low luminescence branching ratio for the ${}^3\text{H}_4 \rightarrow {}^3\text{H}_5$ transition [15], (ii) multi-phonon non-radiative (NR) relaxation from this state in high-phonon energy (oxide) host materials, (iii) strong self-quenching of the luminescence lifetime with Tm doping due to an efficient cross-relaxation (CR) process, ${}^3\text{H}_4(\text{Tm}_1) + {}^3\text{H}_6(\text{Tm}_2) \rightarrow {}^3\text{F}_4(\text{Tm}_1) + {}^3\text{F}_4(\text{Tm}_2)$, for neighboring Tm^{3+} ions [18], (iv) energy-migration to impurities from the ${}^3\text{H}_4$ state at high Tm^{3+} doping levels [19], and (v) highly probable colasing on the high-gain ${}^3\text{F}_4 \rightarrow {}^3\text{H}_6$ transition. The advantage of $\sim 2.3 \mu\text{m}$ lasers based on Tm^{3+} ions (as compared to other sources emitting in this spectral range) is the availability of pump sources (e.g., AlGaAs laser diodes [20] whose emission at $\sim 0.8 \mu\text{m}$ well overlaps with an intense and broad ${}^3\text{H}_6 \rightarrow {}^3\text{H}_4$ Tm^{3+} absorption band) and laser gain media (e.g., $\text{Tm}:\text{LiYF}_4$ single-crystals [21] or $\text{Tm}:\text{ZBLAN}$ glass fibers [22]).

The above considerations, however, greatly limited the selection of active gain media for bulk $\sim 2.3 \mu\text{m}$ Tm lasers from the point of view of the host matrix (only low-phonon energy crystals, e.g., fluorides) and the Tm doping level (preferably low, to prevent self-quenching of the ${}^3\text{H}_4$ lifetime). Thus, in most of the previous studies, mainly $\text{Tm}:\text{LiYF}_4$ crystals with relatively low doping levels were studied (see, e.g., [20,21]).

Pinto *et al.* reported on a CW $\text{Tm}:\text{LiYF}_4$ laser delivering 0.22 W at 2.30 μm with a slope efficiency of 15% and achieved a wavelength tuning between 2.20 and 2.46 μm [21]. ML $\text{Tm}:\text{LiYF}_4$ lasers operating on the ${}^3\text{H}_4 \rightarrow {}^3\text{H}_5$ transition were reported in [23,24]. The shortest pulses were achieved by Canbaz *et al.* (514 fs at 2.30 μm) from a Kerr-lens ML laser operating at a repetition rate of 41.5 MHz [24]. The slope efficiency in such lasers has been rather low, well below the Stokes (S) limit of $\eta_{St,L} \approx 34\%$ for $\text{Tm}:\text{LiYF}_4$. Only recently, we showed theoretically [25] and reported experimentally using fluoride crystals [25,26] that the slope efficiency of Tm lasers operating on the ${}^3\text{H}_4 \rightarrow {}^3\text{H}_5$ transition can overcome the S limit and potentially approach $2\eta_{St,L}$ owing to energy-transfer upconversion (ETU), ${}^3\text{F}_4(\text{Tm}_1) + {}^3\text{F}_4(\text{Tm}_2) \rightarrow {}^3\text{H}_6(\text{Tm}_1) + {}^3\text{H}_4(\text{Tm}_2)$, which becomes efficient at moderate Tm doping levels and acts against the CR by refilling the upper laser level. We also suggested that this mechanism may act in other Tm^{3+} -doped crystals.

Note that other pumping schemes for $\sim 2.3 \mu\text{m}$ Tm lasers relying on the photon avalanche mechanism were also proposed, still leading to a relatively low laser efficiency [27,28].

Recently, we revisited well-known Tm^{3+} -doped oxide crystals ($\text{Tm}:\text{Y}_3\text{Al}_5\text{O}_{12}$, $\text{Tm}:\text{YAlO}_3$) regarding their potential for efficient 2.3 μm lasers [29,30]. We demonstrated a watt-level output from a $\text{Tm}:\text{Y}_3\text{Al}_5\text{O}_{12}$ laser operating on the ${}^3\text{H}_4 \rightarrow {}^3\text{H}_5$ transition: 1.07 W at ~ 2.19 and 2.32 μm with a slope efficiency of 46.3% [29]. However, both crystals are known for their relatively long radiative lifetimes of the ${}^3\text{H}_4$ state and moderate multi-phonon NR relaxation from this level. Interestingly, the use of $\text{Tm}:\text{Y}_3\text{Al}_5\text{O}_{12}$ (highest phonon energy of 857 cm^{-1}) raised the question of the role of vibronic emission for wavelengths between 2 and 2.3 μm .

In the present work, we demonstrate power-scalable and highly efficient operation on the ${}^3\text{H}_4 \rightarrow {}^3\text{H}_5$ transition of a Tm laser based on another high-phonon energy oxide host, monoclinic double tungstate, and reveal the effect of the Tm doping concentration on the laser performance. As a material under study, we selected Tm^{3+} -doped $\text{KLu}(\text{WO}_4)_2$ [31]. So far, this crystal has been extensively studied for CW [32], Q-switched [33], and fs ML [34] lasers emitting at $\sim 2 \mu\text{m}$. Its spectroscopic features are high absorption and stimulated-emission (SE) cross sections for polarized light, broad and intense emission bands, high quantum yield, and weak concentration-quenching of the luminescence from the ${}^3\text{F}_4$ state, and efficient CR [14]. The host matrix also provides nearly athermal behavior for certain crystal cuts, thus allowing for power scaling [32]. $\text{KLu}(\text{WO}_4)_2$ is known as a Raman-active material [35] with yet higher maximum phonon energy $h\nu_{ph}$ of $\sim 907 \text{cm}^{-1}$. Thus, the energy-gap law for the multi-phonon NR relaxation postulating that the rate of NR relaxation is weak if $\Delta E > 4 h\nu_{ph}$ (ΔE is the energy-gap to the lower-lying multiplet) [36] is valid for both the ${}^3\text{H}_4$ and ${}^3\text{F}_4$ states [Fig. 1(a)]. So far, $\sim 2.3 \mu\text{m}$ lasing from $\text{Tm}:\text{KLu}(\text{WO}_4)_2$ or its Tm^{3+} -doped isomorphs $\text{KGd}(\text{WO}_4)_2$ and $\text{KY}(\text{WO}_4)_2$ has never been demonstrated.

2. CRYSTAL GROWTH

The growth of $\text{Tm}:\text{KLu}(\text{WO}_4)_2$ crystals was addressed before [31]. Here, we briefly mention the key details. The crystals were grown by the top seeded solution growth slow-cooling

102
103
104
105
106
107
108
109
110
111
112
113
114
115
116
117
118
119
120
121
122
123
124
125
126
127
128
129
130
131
132
133
134
135
136
137
138
139
140
141
142
143
144
145
146
147
148
149
150
151
152
153
154
155
156
157
158

Table 1. Parameters of the Thulium-Doped Laser Elements

Doping, at. %	N_{Tm} , 10^{20} cm^{-3}	t , mm	Aperture, mm^2
0.5	0.35	9.30 (N_g)	2.56(N_m) \times 3.12(N_p)
1.5	1.14	5.97 (N_g)	3.72(N_m) \times 4.10(N_p)
3.0	2.41	4.91 (N_g)	3.73(N_m) \times 4.09(N_p)

(TSSG SC) method from the flux using potassium ditungstate ($\text{K}_2\text{W}_2\text{O}_7$) as a solvent [31]. An undoped seed oriented along the [010] direction was used to start the growth. The growth was performed in Pt crucibles using K_2CO_3 , WO_3 , Lu_2O_3 , and Tm_2O_3 reagents. The concentration of Tm^{3+} ions was 0.5, 1.5, or 3.0 at. %. The temperature gradient in the solution was ~ 1 K/cm, the rotation speed of the seed was 40 rpm, and the cooling rate was 0.1–0.3 K/h. The crystals had a slight pale-yellow coloration due to the Tm^{3+} doping. The actual Tm^{3+} doping concentration N_{Tm} in the crystals was determined by electron probe microanalysis (EPMA); see Table 1.

$\text{Tm} : \text{KLu}(\text{WO}_4)_2$ belongs to the monoclinic crystal class (sp. gr. $C_{2h}^6 - C2/c$, No. 15). The lattice constants for 3 at. % Tm doping are $a = 10.576 \text{ \AA}$, $b = 10.215 \text{ \AA}$, $c = 7.487 \text{ \AA}$, and the monoclinic angle $\beta = 130.68^\circ$ [14]. This crystal is optically biaxial. Its optical indicatrix was deeply characterized before [31,37]. Briefly, the three optical indicatrix axes (N_p , N_m and N_g) are selected according to the convention $n_p < n_m < n_g$ for the principal refractive indices, and are oriented as follows: the N_p axis is parallel to the b axis (the C_2 symmetry axis), and the N_m and N_g ones are lying in the $a-c$ plane ($\perp C_2$, the mirror plane). The angle $N_g^c = 18.5^\circ$, measured outside the monoclinic angle β [31]. At the wavelength of $\sim 2.3 \mu\text{m}$, the principal refractive indices calculated using the Sellmeier equations [37] are $n_p = 1.984$, $n_m = 2.014$, and $n_g = 2.061$.

The rectangular laser elements were all oriented for light propagation along the N_g axis (N_g cut). This is because of two reasons. First, this crystal cut provides attractive thermo-optic properties (weak, positive, and nearly spherical thermal lens [32]). Second, it gives access to the polarizations $E \parallel N_m$ and $E \parallel N_p$ corresponding to intense spectral bands both in absorption and emission [14]. The sample thickness (t) and aperture are listed in Table 1. Both input and output facets ($N_m \times N_p$) were polished to laser quality and remained uncoated.

3. NEAR- AND MIR-INFRA-RED EMISSIONS

A. Stimulated-Emission Cross sections

The SE cross sections for the ${}^3\text{F}_4 \rightarrow {}^3\text{H}_6$ transition (at $\sim 1.9 \mu\text{m}$) of Tm^{3+} ions in $\text{KLu}(\text{WO}_4)_2$ were reported before [31]. Here, we mainly focus on thulium emission originating from the ${}^3\text{H}_4$ state and suitable for laser operation, i.e., ${}^3\text{H}_4 \rightarrow {}^3\text{F}_4$ (at $\sim 1.5 \mu\text{m}$) and ${}^3\text{H}_4 \rightarrow {}^3\text{H}_5$ (at $\sim 2.3 \mu\text{m}$). We also briefly characterize the ${}^3\text{F}_4 \rightarrow {}^3\text{H}_6$ transition as it spectrally partially overlaps with the desired SWIR one.

First, polarized luminescence spectra $W_i(\lambda)$, where $i = p, m, g$ represents the polarization index, were measured. As an excitation source, we used a Ti:sapphire laser tuned to $\sim 802 \text{ nm}$. The spectra at $\sim 1.5 \mu\text{m}$ and $\sim 1.9 \mu\text{m}$ were measured using an optical spectrum analyzer (OSA, AQ6375B, Yokogawa, spectral bandwidth, $\text{SBW} = 1 \text{ nm}$). To measure

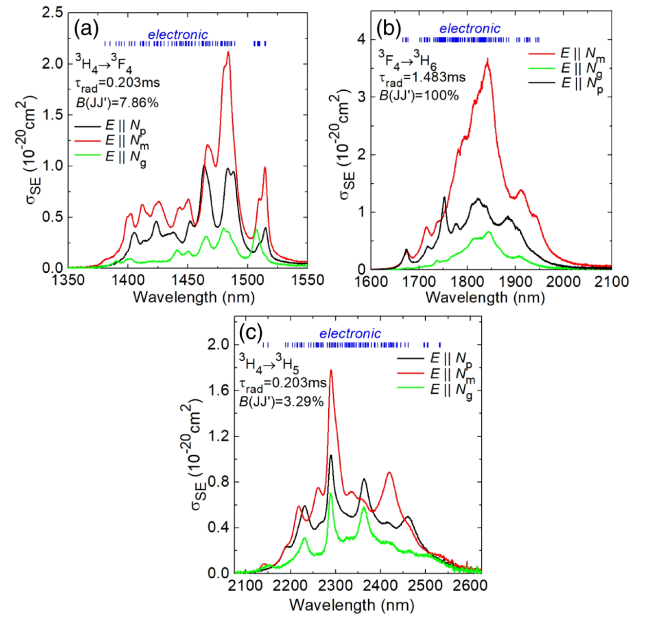


Fig. 2. Stimulated-emission (SE) cross sections, σ_{SE} , for (a) ${}^3\text{H}_4 \rightarrow {}^3\text{F}_4$, (b) ${}^3\text{F}_4 \rightarrow {}^3\text{H}_6$, and (c) ${}^3\text{H}_4 \rightarrow {}^3\text{H}_5$ transitions of Tm^{3+} in monoclinic $\text{KLu}(\text{WO}_4)_2$ for light polarizations $E \parallel N_p$, N_m and N_g , calculated using the F–L formula, Eq. (1). Vertical dashes indicate all possible purely electronic transitions between the Stark sub-levels of the involved multiplets.

the spectra at $\sim 2.3 \mu\text{m}$, we used a 0.6 m monochromator (HRS2, Jobin-Yvon, resolution: 4.5 nm), a lock-in amplifier (SR810 DSP, Stanford Research Systems), and an InSb photodetector (J10D series, Judson Infrared) cooled by liquid N_2 . A Glan–Taylor polarizer was employed for polarized studies. The wavelength calibration was performed using an Hg lamp (Schwabe), and the response of the setup was calibrated using a 20 W quartz iodine lamp so that the measured spectra $W_i(\lambda)$ could be calibrated for the spectral response of the setup for the specific polarization yielding the calibrated spectra $W'_i(\lambda)$.

The SE cross sections, σ_{SE} , were calculated using the Füchtbauer–Ladenburg (F–L) formula [38],

$$\sigma_{SE}^i(\lambda) = \frac{\lambda^5}{8\pi \langle n \rangle^2 \tau_{rad} c} \frac{W'_i(\lambda) B(JJ')}{\sum_{j=p,m,g} \int \lambda W'_j(\lambda) d\lambda}, \quad (1)$$

where λ is the light wavelength, $\langle n \rangle$ is the mean refractive index at the mean emission wavelength (λ_{em}), c is the speed of light, τ_{rad} is the radiative lifetime of the emitting state (${}^3\text{H}_4$ or ${}^3\text{F}_4$), and $B(JJ')$ is the luminescence branching ratio. We used the transition probabilities for Tm^{3+} determined by the Judd–Ofelt theory according to the intensity parameters $\Omega_2 = 9.01$, $\Omega_4 = 1.36$, and $\Omega_6 = 1.43 [10^{-20} \text{ cm}^2]$, namely $\tau_{rad}({}^3\text{F}_4) = 1.483 \text{ ms}$, $\tau_{rad}({}^3\text{H}_4) = 0.203 \text{ ms}$, and $B({}^3\text{H}_4 \rightarrow {}^3\text{F}_4) = 7.86\%$, $B({}^3\text{H}_4 \rightarrow {}^3\text{H}_5) = 3.29\%$ [14]. The refractive indices were calculated from the Sellmeier equations [37]. The results are shown in Fig. 2.

The $\text{Tm} : \text{KLu}(\text{WO}_4)_2$ crystal exhibits a strong polarization-anisotropy of the SE cross sections for all the studied transitions. For the peak σ_{SE} values, the following relation is observed: $\sigma_{SE}(m) > \sigma_{SE}(p) > \sigma_{SE}(g)$. This anisotropy stems from the

low symmetry of the rare-Earth site in the $\text{KLu}(\text{WO}_4)_2$ host matrix (C_2). For each of the considered transitions, we calculated the wavelengths of all the possible purely electronic transitions between the Stark components of the involved multiplets using the reported crystal-field splitting [14]. They are shown as dashes in Fig. 2 and facilitate the assignment of the observed emissions.

For the ${}^3\text{H}_4 \rightarrow {}^3\text{F}_4$ transition, the emission band spans from 1.38 to 1.52 μm (according to the calculated electronic transitions) and the maximum $\sigma_{SE} = 2.11 \times 10^{-20} \text{ cm}^2$ at 1483 nm for the light polarization $\mathbf{E} \parallel N_m$.

For the ${}^3\text{F}_4 \rightarrow {}^3\text{H}_6$ transition, the emission band is much broader due to the relatively large total Stark splitting of the ground-state (${}^3\text{H}_6$), and it spans from 1.67 to 1.95 μm (the electronic transitions), while the vibronic tail of the emission band extends beyond $\sim 2 \mu\text{m}$. The maximum σ_{SE} reaches $3.57 \times 10^{-20} \text{ cm}^2$ at 1842 nm for $\mathbf{E} \parallel N_m$. The ${}^3\text{F}_4 \rightarrow {}^3\text{H}_6$ transition represents a quasi-three-level laser scheme with reabsorption. Thus, the laser emission is typically achieved at longer wavelengths. In particular, $\sigma_{SE} = 0.91 \times 10^{-20} \text{ cm}^2$ at 1946 nm for $\mathbf{E} \parallel N_m$. At this emission wavelength, the anisotropy of the SE cross sections is expressed by the ratios $\sigma_{SE}(m) : \sigma_{SE}(p) = 3.7$ and $\sigma_{SE}(m) : \sigma_{SE}(g) = 11$. This imposes the emission to be linearly polarized in $\text{Tm} : \text{KLu}(\text{WO}_4)_2$ lasers. The determined σ_{SE} values agree with those calculated by the reciprocity method [31].

Finally, for the transition of interest in this work, namely ${}^3\text{H}_4 \rightarrow {}^3\text{H}_5$, the emission band is also rather broad and spans from 2.14 to 2.53 μm (the electronic transitions). The laser wavelength for this quasi-four-level laser scheme is simply determined by the SE cross section spectra. The maximum σ_{SE} is $1.78 \times 10^{-20} \text{ cm}^2$ at 2289 nm, and the corresponding emission bandwidth $\Delta\lambda_{em}$ (determined as the full width at half-maximum, FWHM) is 32.1 nm for $\mathbf{E} \parallel N_m$. The anisotropy of the SE cross sections is weaker than for the ${}^3\text{F}_4 \rightarrow {}^3\text{H}_6$ transition, i.e., $\sigma_{SE}(m) : \sigma_{SE}(p) = 1.7$ and $\sigma_{SE}(m) : \sigma_{SE}(g) = 2.5$; however, it is enough to ensure natural selection of the laser polarization. The determined SE cross section for the ${}^3\text{H}_4 \rightarrow {}^3\text{H}_5$ transition is higher than in any previously studied Tm^{3+} -doped fluoride or oxide crystal, and is assigned to the strong polarization-anisotropy of the optical properties in $\text{Tm} : \text{KLu}(\text{WO}_4)_2$, and in part, to the relatively short radiative lifetime of the emitting state (${}^3\text{H}_4$). Indeed, for the most widespread crystal for $\sim 2.3 \mu\text{m}$ lasers, $\text{Tm} : \text{LiYF}_4$, σ_{SE} reaches $0.57 \times 10^{-20} \text{ cm}^2$ at 2305 nm, and $\Delta\lambda_{em}$ is 25.8 nm for π -polarized light [25]. Considering the relatively broad emission band, $\text{Tm} : \text{KLu}(\text{WO}_4)_2$ appears to be attractive for ML lasers at $\sim 2.3 \mu\text{m}$.

B. Vibronic Contribution

As can be seen from Figs. 2(b) and 2(c), the spectral ranges of purely electronic ${}^3\text{F}_4 \rightarrow {}^3\text{H}_6$ and ${}^3\text{H}_4 \rightarrow {}^3\text{H}_5$ transitions do not overlap. However, it is known that all Tm^{3+} -doped materials exhibit strong electron-phonon (vibronic) interaction leading to the broadening of their emission bands. For Tm^{3+} , this is determined by its location almost in the end of the lanthanide series [39,40]. Besides the broadening of the emission peaks corresponding to the particular Stark-to-Stark transitions, the

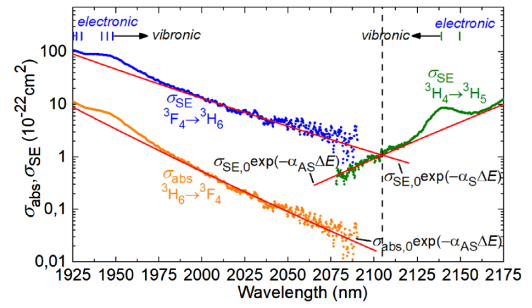


Fig. 3. Electron-phonon coupling bridges the gap between the ${}^3\text{F}_4 \rightarrow {}^3\text{H}_6$ and ${}^3\text{H}_4 \rightarrow {}^3\text{H}_5$ electronic transitions of Tm^{3+} in monoclinic $\text{KLu}(\text{WO}_4)_2$ crystal: a semi-logarithmic plot of the stimulated-emission, σ_{SE} , and absorption, σ_{abs} , cross sections for the ${}^3\text{F}_4 \leftrightarrow {}^3\text{H}_6$ and ${}^3\text{H}_4 \rightarrow {}^3\text{H}_5$ transitions for light polarization $\mathbf{E} \parallel N_m$. Symbols, experimental data; lines, exponential fits to the phonon sidebands of the spectral bands, Eq. (2). Vertical dashes indicate the purely electronic transitions between the Stark sub-levels of the involved multiplets. Black vertical dashed line indicates the wavelength of equal σ_{SE} for the two transitions.

electron-phonon coupling determines the shape of the vibronic tails of the emission bands corresponding to S and anti-Stokes (AS) processes [41]. The AS vibronic tail is the one observed at wavelengths below the shortest wavelength of the pure electronic transition (occurring between the highest sub-level of the emitting multiplet and the lowest sub-level of the terminating one). The S vibronic tail is observed at wavelengths above the longest wavelength of the pure electronic transition (occurring between the lowest sub-level of the emitting multiplet and the highest sub-level of the terminating one). The S vibronic tail of the ${}^3\text{F}_4 \rightarrow {}^3\text{H}_6$ transition and the AS one of the ${}^3\text{H}_4 \rightarrow {}^3\text{H}_5$ transition may overlap. This raises the question of attributing the emission occurring at intermediate wavelengths.

The analysis of the possible overlap of the ${}^3\text{F}_4 \rightarrow {}^3\text{H}_6$ and ${}^3\text{H}_4 \rightarrow {}^3\text{H}_5$ emissions of Tm^{3+} ions in $\text{KLu}(\text{WO}_4)_2$ is performed in Fig. 3 in terms of the SE cross section spectra plotted in a semi-log scale. For the ${}^3\text{F}_4 \rightarrow {}^3\text{H}_6$ transition, the longest wavelength of the electronic transition is 1948 nm (occurring between the Stark sub-levels 5663 cm^{-1} (${}^3\text{F}_4$) and 530 cm^{-1} (${}^3\text{H}_6$) [14]). For the ${}^3\text{H}_4 \rightarrow {}^3\text{H}_5$ one, the shortest wavelength of the electronic transition is 2139 nm (occurring between the Stark sub-levels 12906 cm^{-1} (${}^3\text{H}_4$) and 8231 cm^{-1} (${}^3\text{H}_5$) [14]). The vibronic tails are well fitted with the exponential law [42],

$$\sigma_S = \sigma_0 \exp(-\alpha_S \Delta E), \quad (2a)$$

$$\sigma_{AS} = \sigma_0 \exp(-\alpha_{AS} \Delta E), \quad (2b)$$

where ΔE is the energy mismatch between the vibronic and the electronic transition, σ_0 is the transition cross section at the photon energy corresponding to the electronic transition, and the factors α_S and α_{AS} depend on the host material. For $\text{Tm} : \text{KLu}(\text{WO}_4)_2$, we obtain the material-dependent factors $\alpha_S = 10.0 \pm 0.7 \times 10^{-3} \text{ cm}^{-1}$ and $\alpha_{AS} = 14.5 \pm 1.5 \times 10^{-3} \text{ cm}^{-1}$. The wavelength at which the SE cross sections for both transitions are equal is $\lambda_{eq} = 2104 \pm 10 \text{ nm}$.

Thus, the gap between the ${}^3F_4 \rightarrow {}^3H_6$ and ${}^3H_4 \rightarrow {}^3H_5$ electronic transitions of Tm^{3+} in $KLu(WO_4)_2$ is bridged by vibronic transitions. The performed analysis allowed us to propose a criterion for the attribution of emissions within this gap. All the emissions with wavelengths exceeding λ_{eq} will be assigned as such related to the ${}^3H_4 \rightarrow {}^3H_5$ transition (either of electronic or vibronic nature), and all the emissions at shorter wavelengths to the ${}^3F_4 \rightarrow {}^3H_6$ one.

Let us discuss previously obtained results on Tm: $KLu(WO_4)_2$ lasers in light of this criterion. Typically, bulk lasers based on this crystal operated at a wavelength of $\sim 1.94 \mu m$, e.g., Serres *et al.* reported on a diode-pumped 3 at. % Tm-doped laser delivering multi-watt output at 1946 nm [32]. This wavelength is close to the longest wavelength of the ${}^3F_4 \rightarrow {}^3H_6$ purely electronic transition.

Longer wavelengths were achieved under two circumstances. First, highly doped crystals provided emission above $2 \mu m$ using low output coupling and without any spectrally selective elements: Mateos *et al.* reported a 0.59 W output power at 2005–2045 nm with a slope efficiency of 51% for 15 at. % Tm doping [43]. Such wavelengths clearly represent vibronic emission. This behavior was mainly induced by the high Tm^{3+} doping concentration as a lower inversion ratio was needed to ensure the gain needed to compensate for the losses. For small inversion ratios, the gain spectra for the quasi-three-level ${}^3F_4 \rightarrow {}^3H_6$ transition are flat and broad extending beyond $2 \mu m$.

3 Second, long laser wavelengths were achieved in bulk Tm lasers employing a spectrally selective output coupler (OC) providing high transmission (HT) at $< 2 \mu m$: Loiko *et al.* reported on a diode-pumped 3 at. % Tm: $KLu(WO_4)_2$ laser delivering 1.17 W with a slope efficiency of 39% at 2109–2133 nm [44], the longest wavelength achieved so far with this material. Besides the assignment of this emission to the vibronic mechanism, the authors suggested a resonant mechanism involving low-frequency Raman modes of the host matrix (a possible contribution of CW self-Raman conversion). Note that the use of a similar cavity mirror allowed the authors in [34] to operate a ML Tm: $KLu(WO_4)_2$ laser above $2 \mu m$ (at 2037 nm) avoiding the unwanted structured water vapor atmospheric absorption and achieving fs pulse duration.

According to the proposed criterion, the emission at 2109–2133 nm observed in [44] can be in part assigned to the ${}^3H_4 \rightarrow {}^3H_5$ transition (the vibronic contribution). Probably because of the limited reflection band of the cavity mirrors in [44], the authors were unable to achieve laser emission at longer wavelengths corresponding to the electronic ${}^3H_4 \rightarrow {}^3H_5$ transition.

C. Lifetime of the 3H_4 Multiplet: An Overview

The luminescence dynamics for Tm^{3+} ions in $KLu(WO_4)_2$ was studied previously. In this section, we aim to summarize the reported results and to analyze them concerning the targeted ${}^3H_4 \rightarrow {}^3H_5$ transition, i.e., by focusing on the 3H_4 multiplet. The intrinsic lifetime τ_{30} determined in the limit of a very low Tm concentration (thus not being affected by the CR and energy-migration) is in general shorter than the radiative one because of the multi-phonon NR relaxation [45,46],

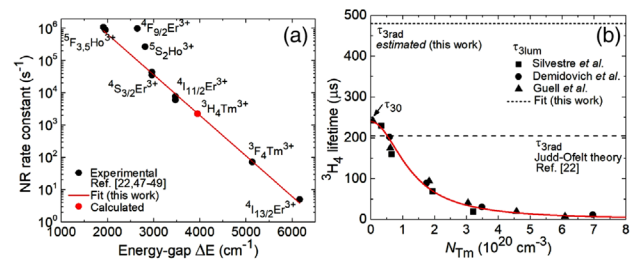


Fig. 4. (a) Rate constants of multi-phonon non-radiative relaxation W_{NR} versus the energy-gap to the lower-lying state ΔE for various excited states of rare-Earth ions in monoclinic double tungstate crystals: circles, data from [14,47–49]; red line, fit using Eq. (3b); red circle, estimation for the ${}^3H_4Tm^{3+}$ state. (b) Luminescence lifetimes of the ${}^3H_4Tm^{3+}$ state in monoclinic double tungstate crystals: symbols, data from [14,50,51]; red curve, fit using Eq. (4a); horizontal dashed lines, estimations of the radiative lifetime (this work and [14]).

$$\frac{1}{\tau_{30}} = \frac{1}{\tau_{3rad}} + W_{NR}, \quad (3a)$$

$$W_{NR} = C e^{-\alpha \Delta E}, \quad (3b)$$

where W_{NR} is the rate constant (expressed in $[s^{-1}]$) of the multi-phonon NR relaxation, which depends on the energy-gap to the lower-lying state ΔE and the maximum phonon energy $h\nu_{pb}$, and C and α are characteristic constants for the material. C has the meaning of a NR rate constant in the limit of zero energy-gap ($\Delta E \rightarrow 0$), and $\alpha = -\ln(\epsilon)/(h\nu_{pb})$, where ϵ is the ratio between the probabilities of m -phonon and $m-1$ -phonon relaxation.

In Fig. 4(a), we analyzed the W_{NR} values calculated by comparing the radiative and intrinsic lifetimes of various excited states of several rare-Earth ions in several $KRE(WO_4)_2$ crystals [14,47–49] considering their very close phonon spectra. The experimental data on W_{NR} are well fitted with Eq. (3b) yielding the following best-fit material parameters: $C = 2.14 \pm 2 \times 10^8 s^{-1}$ and $\alpha = 2.90 \pm 0.1 \times 10^{-3} cm$. These parameters reasonably agree with those estimated by de Mendivil *et al.* [47].

Regarding the ${}^3H_4Tm^{3+}$ state, according to the Judd-Ofelt analysis by Silvestre *et al.* [14], the radiative lifetime $\tau_{3rad} = 0.203 ms$. This obviously contradicts the luminescence lifetime measured by the same authors for the low doped sample (0.5 at. % Tm), $\tau_{3lum} = 0.230 ms$ [14], which can be approximately taken as the intrinsic one. The application of Eq. (3b) with the material parameters determined above yields $W_{NR} = 2.2 \pm 1 \times 10^3 s^{-1}$ and, accordingly, τ_{3rad} about 0.47 ms. The difference between this value and the one obtained from the Judd-Ofelt calculations can be explained by the error in the latter. At the moment, we are unable to clarify this discrepancy, and further analysis is needed (e.g., by employing the modified Judd-Ofelt theory accounting for the configuration interaction).

The luminescence lifetime of the 3H_4 state can be represented as a function of the Tm doping concentration (neglecting the energy-migration) [18,52],

$$\frac{1}{\tau_{3lum}} = \frac{1}{\tau_{30}} + W_{CR}, \quad (4a)$$

382

383

384

385

386

387

388

389

390

391

392

393

394

395

396

397

398

399

400

401

402

403

404

405

406

407

408

409

410

411

412

413

414

415

416

325

326

327

328

329

330

331

332

333

334

335

336

337

338

339

340

341

342

343

344

345

346

347

348

349

350

351

352

353

354

355

356

357

358

359

360

361

362

363

364

365

366

367

368

369

370

371

372

373

374

375

376

377

378

379

380

381

417

$$W_{CR} = C_{CR} N_{Tm}^2 \quad (4b)$$

418 Here, W_{CR} is the CR rate constant (expressed in $[s^{-1}]$), and C_{CR}
 419 is the concentration-independent CR parameter (expressed
 420 in $[cm^6 s^{-1}]$). In Fig. 4(b), we summarize the luminescence
 421 lifetimes of the 3H_4 multiplet of Tm^{3+} ions reported for
 422 $KLu(WO_4)_2$ and its isomorph crystals [14,50,51]. In this
 423 analysis, we accounted for the different cation density per
 424 1 at. % doping in different crystals. As can be seen, for different
 425 host-forming cations in the monoclinic double tungstate
 426 crystals, the 3H_4 lifetime of the dopant ones (Tm^{3+}) follows
 427 nearly the same trend. The fitting of the experimental data using
 428 Eq. (4) yields the following parameters: $\tau_{30} = 0.24 \pm 0.01$ ms
 429 and $C_{CR} = 2.70 \pm 0.15 \times 10^{-37} cm^6 s^{-1}$. These values are in
 430 reasonable agreement with those published in [18].

431 The use of Eq. (4a) with the determined best-fit τ_{30} and C_{CR}
 432 parameters yields $\tau_{3lum} = 222, 130,$ and $50 \mu s$ for the 0.5, 1.5,
 433 and 3.0 at.% Tm^{3+} -doped $KLu(WO_4)_2$ crystals, respectively.

434 4. LASER PERFORMANCE

435 A. Laser Setup

436 The scheme of the laser setup is shown in Fig. 5(a). A simple
 437 linear nearly hemispherical cavity was used. It comprised
 438 a flat pump mirror (PM) coated for HT ($T = 95.3\%$) at
 439 $0.77\text{--}0.81 \mu m$ and for high reflection (HR, $R > 99.9\%$) at
 440 $2.12\text{--}2.50 \mu m$, and a set of concave OCs all having the same
 441 radii of curvature (RoC) of 100 mm and a measured transmission
 442 T_{OC} at $2.18\text{--}2.35 \mu m$ of 0.1% ($\pm 0.05\%$), 0.7%, 1.3%,
 443 or 4.0% ($\pm 0.2\%$). The OCs, except the 0.1% one, provided
 444 high reflectivity ($R > 97\%$) at the pump wavelength. In order
 445 to suppress the unwanted ${}^3F_4 \rightarrow {}^3H_6$ transition, all the OCs
 446 provided HT ($T > 90\%$) at $1.80\text{--}1.98 \mu m$. Note that no special
 447 requirements were applied for the PM, and its reflectivity at
 448 $\sim 1.95 \mu m$ was $R \sim 93\%$. The total geometrical cavity length
 449 was ~ 100 mm.

450 Three laser crystals with Tm doping levels of 0.5, 1.5, and
 451 3.0 at. % were employed (see Table 1). All of them were N_g

452 cut. The crystals were mounted on a massive passively cooled
 453 Cu-holder using a silver thermal paste for better heat removal.
 454 The laser crystals were placed close to the PM leaving only a
 455 small air gap (less than 1 mm).

456 As a pump source, we employed a CW Ti:sapphire laser
 457 (3900S, Spectra Physics) delivering up to 3.6 W at the wave-
 458 lengths of $770\text{--}810$ nm (tunable output) in the fundamental
 459 mode ($M^2 \approx 1$). The pump wavelength thus corresponded to
 460 the ${}^3H_6 \rightarrow {}^3H_4$ Tm^{3+} transition. The incident pump power
 461 was adjusted using a half-wave plate and a Glan–Taylor polarizer
 462 oriented in such a way that the pump polarization corresponded
 463 to $E_p || N_p$ or $E_p || N_m$ in the crystal. The pump beam was
 464 expanded using a homemade telescope (reimaging ratio, 1:2)
 465 and focused into the crystal using an achromatic lens (focal
 466 length, $f = 60$ mm). A mechanical chopper (frequency, 20 Hz;
 467 duty cycle, 1:2) was introduced in the beam path to ensure
 468 quasi-CW pumping reducing the heat loading in the crystal.
 469 The pump spot radius in the focus w_p was $40 \pm 10 \mu m$
 470 (at the $1/e^2$ level, as measured by the optical knife method),
 471 and the calculated confocal parameter of the pump beam $2z_R$
 472 exceeded 10 mm (in the crystal). The radius of the laser mode
 473 in the crystal was calculated by the ABCD-method account-
 474 ing for the positive thermal lens to be $w_L = 40\text{--}44 \pm 5 \mu m$
 475 (slowly decreasing with the pump power). Thus, relatively good
 476 mode-matching was observed.

477 For each crystal, first, we measured pump absorption under
 478 non-lasing (NL) conditions in a single-pass. The measurements
 479 were done for the pump wavelengths of 793.8 and 802.1 nm
 480 corresponding to the polarizations $E_p || N_p$ or $E_p || N_m$,
 481 respectively. Then, the second pass of the pump was taken into
 482 account leading to the total value $\eta_{abs,NL(2-pass)}$ (it does not
 483 include Fresnel losses at the uncoated crystal surfaces). The
 484 decreasing $\eta_{abs,NL(2-pass)}$ value with the incident pump power,
 485 as shown in Figs. 5(b) and 5(c), represents the effect of ground-
 486 state bleaching (absorption saturation). The absorption under
 487 lasing (L) conditions was estimated from the $\eta_{abs,NL(2-pass)}$ value
 488 for each OC at the threshold pump power.

489 To separate the ${}^3H_4 \rightarrow {}^3H_5$ laser emission from the residual
 490 (non-absorbed) pump, we used a bandpass filter (FB2250-500,
 491 Thorlabs). The spectra of the laser emission were measured
 492 using an OSA (AQ6375B, Yokogawa; resolution, 0.2 nm). The
 493 pump wavelength was determined using another OSA (Ando
 494 AQ6315-E; resolution, 0.1 nm). The laser beam profile in the
 495 far-field was captured using a pyroelectric camera (PY-III-HR-
 496 C-A, Ophir). The beam quality factors $M_{x,y}^2$ were measured
 497 by an ISO-standard method using a single spherical CaF_2 lens
 498 ($f = 100$ mm) placed after the OC.

499 In addition to the laser experiment on the ${}^3H_4 \rightarrow {}^3H_5$ tran-
 500 sition, we studied the performance of the 3.0 at. % Tm-doped
 501 crystal on the ${}^3F_4 \rightarrow {}^3H_6$ transition. For this, the same setup
 502 was used, only the cavity mirrors were replaced. The flat PM
 503 provided HT ($T = 97.4\%$) at $\sim 0.79 \mu m$ and HR at 1.87--
 504 $2.30 \mu m$, and the concave OCs (RoC = -100 mm) provided
 505 T_{OC} of 0.5%–15% at $1.90\text{--}2.08 \mu m$. The OCs provided rela-
 506 tively HT of $T > 70\%$ at the pump wavelength, so that the
 507 pumping was in a single-pass in this case.

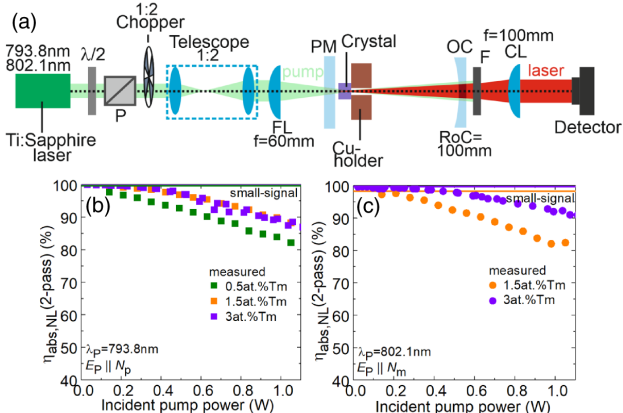


Fig. 5. (a) Scheme of the Tm laser operating on the ${}^3H_4 \rightarrow {}^3H_5$ transition: $\lambda/2$, half-wave plate; P, Glan–Taylor polarizer; FL and CL, focusing and collimating lenses, respectively; PM, pump mirror; OC, output coupler; F, bandpass filter. (b) and (c) Total (double-pass) pump absorption under non-lasing conditions $\eta_{abs,NL(2-pass)}$ for the studied laser crystals. The pump polarization is (b) $E_p || N_p$ and (c) $E_p || N_m$.

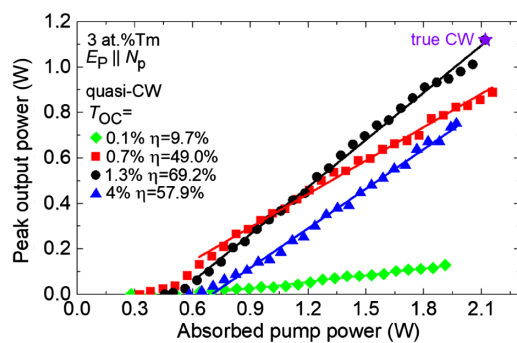


Fig. 6. Input-output dependences for the Tm laser pumped at 793.8 nm ($E_p || N_p$) and operating on the ${}^3H_4 \rightarrow {}^3H_5$ transition in the quasi-CW mode (duty cycle, 1:2); η , slope efficiency. Tm doping, 3 at. %. The asterisk indicates the maximum power obtained in true CW regime ($T_{OC} = 1.3\%$).

B. ${}^3H_4 \rightarrow {}^3H_5$ Transition: Best-Performing Crystal

At first, we report the results achieved with the best-performing crystal (3 at. % Tm doping), the optimum pump polarization ($E_p || N_p$), and the corresponding pump wavelength λ_p of 793.8 nm. We will specify the peak output power obtained by multiplying the average output power by a factor of $\times 2$. This factor was confirmed in experiments in true CW regime performed at low pump powers. For the specified pump conditions, the pump absorption under lasing conditions $\eta_{abs,L(2-pass)}$ decreased with the output coupling from 96.9% ($T_{OC} = 0.1\%$) to 89.4% ($T_{OC} = 4\%$). For all OCs, no colasing at wavelengths below 2 μm (the ${}^3F_4 \rightarrow {}^3H_6$ electronic transition) was observed, verified by spectral measurements in the 1.7–2.4 μm range.

The power characteristics of the laser are shown in Fig. 6. It generated a maximum peak output power of 1.12 W at ~ 2.22 and 2.29 μm (multi-color emission) with a slope efficiency η of 69.2% (determined with respect to the absorbed pump power P_{abs}). The laser threshold was at $P_{th} = 0.45$ W, and the optical-to-optical efficiency, calculated with respect to the pump power incident on the crystal, η_{opt} , reached 44.4% (all characteristics are specified for $T_{OC} = 1.3\%$). The laser threshold gradually increased with T_{OC} , from 0.28 W for the 0.1% OC up to 0.58 W for the 4% OC. The input-output dependences were nonlinear near the laser threshold. No thermal roll-over or fracture of the crystal was observed up to at least $P_{abs} \sim 2$ W.

The true CW laser performance was studied only for the optimum T_{OC} of 1.3%. The input-output dependence was almost identical to that for quasi-CW pumping indicating relatively weak thermal effects for the particular Tm doping level (3 at. % Tm) and output coupling. For the maximum available absorbed pump power P_{abs} of 2.12 W, the CW output power amounted to 1.12 W, as shown by the asterisk in Fig. 6.

The laser generated a linearly polarized output ($E || N_m$) with a polarization degree P exceeding 99%. The polarization state was naturally selected by the anisotropy of the gain in agreement with the SE cross section spectra, cf. Fig. 2(c). The laser emission spectra were dependent both on the output coupling and the pump power, Fig. 7. At low pump powers near the threshold, the laser operated at ~ 2.29 μm for all the studied OCs. This corresponds to the main maximum in the SE cross section

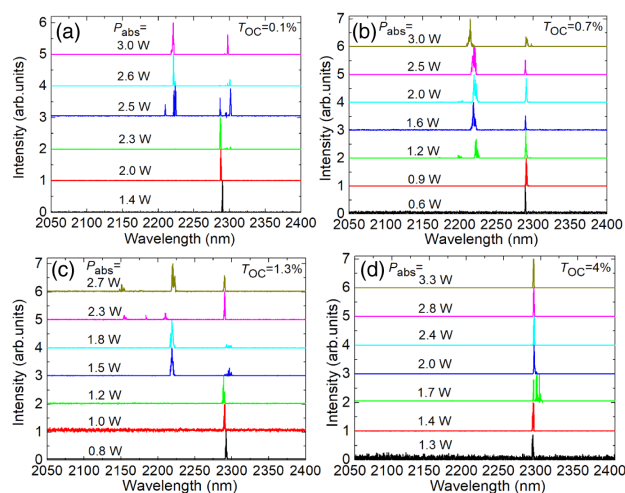


Fig. 7. Emission spectra from the thulium laser (3 at. % Tm) operating on the ${}^3H_4 \rightarrow {}^3H_5$ transition at different absorbed pump powers P_{abs} . Output coupling: (a) 0.1%, (b) 0.7%, (c) 1.3%, and (d) 4.0%. The laser polarization is $E || N_m$.

spectra of Tm : KLu(WO₄)₂. This laser line was maintained with increasing pump power only for the highest studied output coupling ($T_{OC} = 4\%$). For lower T_{OC} , other emission lines appeared at shorter wavelengths (2.14–2.22 μm). A similar behavior was recently observed in another oxide laser crystal, Tm : Y₃Al₅O₁₂ [29].

As pointed out above, the assignment of Tm³⁺ emissions at the intermediate wavelengths of 2.0–2.2 μm may be complicated due to the partial overlap of the ${}^3F_4 \rightarrow {}^3H_6$ and ${}^3H_4 \rightarrow {}^3H_5$ emission bands. The first step is to assign the laser lines to electronic transitions. This was possible for all the observed emission wavelengths assuming transitions between the Stark components of the 3H_4 and 3H_5 multiplets, as shown in Fig. 8, where the transitions are sorted out in the order of increasing wavelength (2139, 2150, 2194, 2214, 2216, 2223, 2287, and 2300 nm). All these emission wavelengths are longer than the λ_{eq} one (2104 nm) defined in Section 3.B. Thus, the observed laser emission can be unambiguously assigned to the ${}^3H_4 \rightarrow {}^3H_5$ transition. Now let us discuss the physical reasons for the multi-color emission at low output couplings. Note that our OCs were supporting laser operation at 2.18–2.35 μm . One reason is the highly probable etalon effect at the PM/crystal interface. This was verified by varying the pump power, which, due to the positive thermal expansion of the crystal in the longitudinal direction, affected the laser spectrum. Another possible reason is the additional gain arising from the vibronic tail of the ${}^3F_4 \rightarrow {}^3H_6$ transition. At such wavelengths, the reabsorption losses are almost negligible. Note that for any Tm laser operating on the ${}^3H_4 \rightarrow {}^3H_5$ transition, a notable fraction of ions is accumulated in the metastable intermediate state (3F_4). If no special attention is paid to suppress the emission at ~ 1.9 μm , colasing at ~ 1.9 μm and 2.3 μm will be observed. In our case, the spectral component below 2 μm is suppressed by the appropriate coatings of the OCs. The third reason is the resonant electron-phonon coupling with the low-frequency Raman modes of the host matrix [44].

The mode profile of the Tm laser in the far-field is shown Fig. 9(a). The output beam was nearly circular, which agrees

508

509

510

511

512

513

514

515

516

517

518

519

520

521

522

523

524

525

526

527

528

529

530

531

532

533

534

535

536

537

538

539

540

541

542

543

544

545

546

547

548

549

550

551

552

553

554

555

556

557

558

559

560

561

562

563

564

565

566

567

568

569

570

571

572

573

574

575

576

577

578

579

580

581

582

583

584

585

586

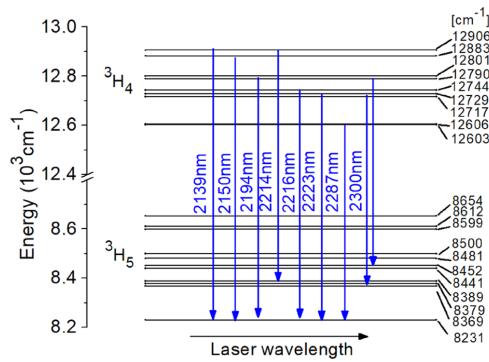


Fig. 8. Crystal-field splitting of the ${}^3\text{H}_4$ and ${}^3\text{H}_5$ multiplets of Tm^{3+} in $\text{KLu}(\text{WO}_4)_2$ crystal (after [14]) and the assignment of the observed laser transitions.

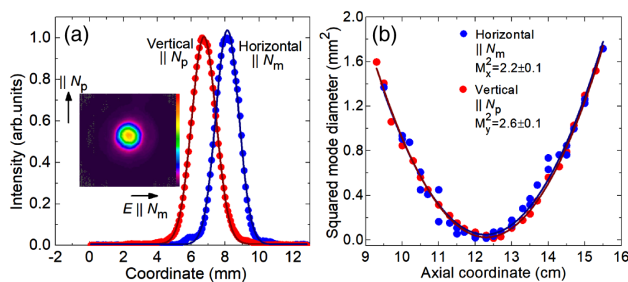


Fig. 9. Spatial characteristics of the output of the Tm laser operating on the ${}^3\text{H}_4 \rightarrow {}^3\text{H}_5$ transition. (a) 1D intensity profiles in the horizontal (x , $\parallel N_m$) and vertical (y , $\parallel N_p$) directions: *symbols*, experimental data; *curves*, Gaussian fits; *inset*, 2D mode profile in the far-field. (b) Evaluation of the beam quality factors $M_{x,y}^2$. Tm doping, 3 at.%. $T_{OC} = 1.3\%$; $P_{abs} = 0.8$ W. The laser polarization ($\mathbf{E} \parallel N_m$) is horizontal.

with the weak astigmatism of the thermal lens in N_g -cut $\text{Tm} : \text{KLu}(\text{WO}_4)_2$ [32]. The 1D intensity profiles in the horizontal (x , $\parallel N_m$) and vertical (y , $\parallel N_p$) directions were fitted with a Gaussian distribution revealing weak mode wings and probably slightly multimode behavior. To clarify that, the beam quality factors $M_{x,y}^2$ were evaluated as shown in Fig. 9(b). They amounted to 2.2 ± 0.1 and 2.6 ± 0.1 , respectively. Thus, despite the high beam quality of the pump radiation ($M^2 \approx 1$), the Tm laser generated a slightly multimode output. We attribute this to two reasons: (i) quasi-four-level nature of the ${}^3\text{H}_4 \rightarrow {}^3\text{H}_5$ transition with no reabsorption and (ii) strong positive (focusing) thermal lens in the $\text{Tm} : \text{KLu}(\text{WO}_4)_2$ crystal. As the thermal lens is pump-dependent, with increasing the pump power, the size of the fundamental mode in the crystal is decreased with respect to the pump spot size and higher-order modes are supported. Note that for $\text{Tm} : \text{KLu}(\text{WO}_4)_2$ lasers operating on the ${}^3\text{F}_4 \rightarrow {}^3\text{H}_6$ transition, an additional mode filtering is provided by reabsorption losses in the wings of the higher-order modes spatially overlapping with unpumped regions of the crystal [18]. This is, however, not the case for the quasi-four-level ${}^3\text{H}_4 \rightarrow {}^3\text{H}_5$ lasing. The possible reabsorption arising from the vibronic sideband of the ${}^3\text{H}_6 \rightarrow {}^3\text{F}_4$ transition is very weak and exponentially decreases with the wavelength, cf. Fig. 3.

C. ${}^3\text{F}_4 \rightarrow {}^3\text{H}_6$ Transition: A Comparison

CW laser operation of $\text{Tm} : \text{KLu}(\text{WO}_4)_2$ crystal on the ${}^3\text{F}_4 \rightarrow {}^3\text{H}_6$ transition was addressed before [31,32]. Here, we studied this laser channel only to provide a direct comparison with the targeted ${}^3\text{H}_4 \rightarrow {}^3\text{H}_5$ transition (such a comparison is performed for the first time).

We implemented the same 3 at. % $\text{Tm} : \text{KLu}(\text{WO}_4)_2$ crystal in a similar cavity with the mirrors coated to support the emission at $\sim 1.9 \mu\text{m}$. The results are shown in Figs. 10(a) and 10(b). The laser generated a maximum output peak power of 0.95 W at 1942–1950 nm with a slope efficiency of 49.8%. The laser threshold was at $P_{th} = 0.13$ W, and η_{opt} was 38.9% (for $T_{OC} = 10\%$). The laser threshold increased with the output coupling, from 0.05 W for $T_{OC} = 0.5\%$ up to 0.19 W for $T_{OC} = 15\%$. The input-output dependences were close to linear. The laser output was linearly polarized ($\mathbf{E} \parallel N_m$), and the spectra were weakly dependent on the pump power. With increasing output coupling, the emission wavelength experienced a slight blueshift, from 1954–1992 nm for $T_{OC} = 0.5\%$ to 1941–1946 nm for $T_{OC} = 15\%$. This behavior is well-known for quasi-three-level Tm lasers and is related to decreasing reabsorption losses at higher inversion in the gain medium associated with higher T_{OC} . Even without spectrally selective mirrors, we were able to observe vibronic emissions for the lowest output coupling (wavelengths above 1948 nm; see Section 3.B).

Previously, a compact (microchip-type) CW 3 at. % $\text{Tm} : \text{KLu}(\text{WO}_4)_2$ laser generated 3.2 W at 1946 nm with a slope efficiency of 50.4% [32]. Better power scaling capabilities as compared to the present work are mainly due to the use of diode-pumping and active (water) cooling of the laser crystal.

In Fig. 10(a), we directly compare the 3 at. % $\text{Tm} : \text{KLu}(\text{WO}_4)_2$ lasers operating on the ${}^3\text{F}_4 \rightarrow {}^3\text{H}_6$ and ${}^3\text{H}_4 \rightarrow {}^3\text{H}_5$ transitions (for the best OC). Surprisingly, the laser operating on the latter transition provides higher peak output power and slope efficiency, albeit at greatly increased laser threshold. The difference in P_{th} is mainly due to the great difference in the intrinsic lifetimes of the upper laser levels, $\tau_{30}({}^3\text{H}_4) = 0.24$ ms (this work) and $\tau_{10}({}^3\text{F}_4) = 1.34$ ms [31].

The slope efficiency of Tm lasers operating on the ${}^3\text{F}_4 \rightarrow {}^3\text{H}_6$ transition is primarily governed by the pump quantum efficiency η_{q1} indicating the number of excitations to the upper laser level (${}^3\text{F}_4$) per number of absorbed pump photons

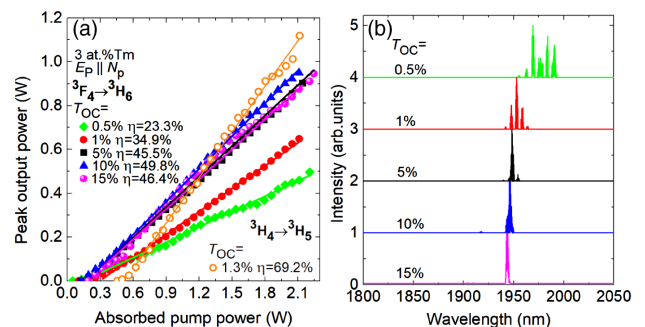


Fig. 10. Tm laser pumped at 793.8 nm ($\mathbf{E}_p \parallel N_p$) and operating on the ${}^3\text{F}_4 \rightarrow {}^3\text{H}_6$ transition in quasi CW mode (duty cycle, 1:2): (a) input-output dependences; η , slope efficiency; the output dependence for the laser operating on the ${}^3\text{H}_4 \rightarrow {}^3\text{H}_5$ transition is given for comparison; (b) typical laser emission spectra measured at $P_{abs} = 0.5$ W. The laser polarization is $\mathbf{E} \parallel N_m$. Tm doping, 3 at. %.

611
612
613
614
615
616
617
618
619
620
621
622
623
624
625
626
627
628
629
630
631
632
633
634
635
636
637
638
639
640
641
642
643
644
645
646
647
648
649
650
651
652

653 at $\sim 0.8 \mu\text{m}$. This parameter depends on the Tm doping
 654 level due to the CR process, ${}^3\text{H}_4(\text{TM}_1) + {}^3\text{H}_6(\text{TM}_2) \rightarrow$
 655 ${}^3\text{F}_4(\text{TM}_1) + {}^3\text{F}_4(\text{TM}_2)$ [18,52],

$$\eta_{q1} = 1 + \frac{W_{\text{CR}}}{(1/\tau_{30}) + W_{\text{CR}}}. \quad (5)$$

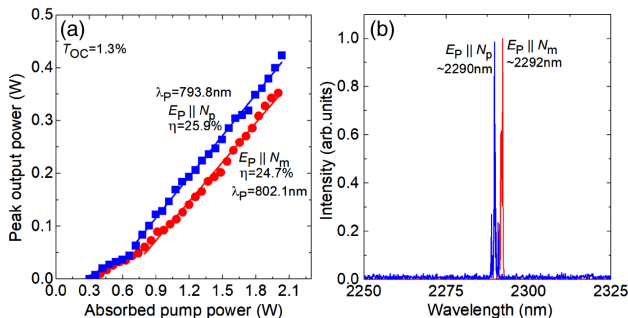
656 Here, W_{CR} is the CR rate constant defined by Eq. (4b), and
 657 C_{CR} is the concentration-independent CR parameter. For
 658 high Tm doping, efficient CR may result in η_{q1} approaching
 659 2 (two-for-one pump process). Thus, the laser slope efficiency
 660 may exceed the S limit under lasing conditions setting the upper
 661 limit of $\eta < 2\eta_{\text{St,L}}$, where $\eta_{\text{St,L}} = \lambda_P/\lambda_L$ and λ_P and λ_L
 662 are the pump and laser wavelengths, respectively. Indeed, very high
 663 η_{q1} value of 1.98 ± 0.02 was observed in a highly doped 15 at.
 664 % Tm : KLu(WO₄)₂ laser emitting at $\sim 1.9 \mu\text{m}$ [43]. For the
 665 case of 3 at. % Tm doping, Eq. (5) yields $\eta_{q1} = 1.79$, which also
 666 explains the high slope efficiency observed in the present work.

667 For the 3 at. % Tm-doped crystal, the round-rip passive cavity
 668 losses were estimated from the Caird analysis [53] to be $L =$
 669 $0.58 \pm 0.2\%$.

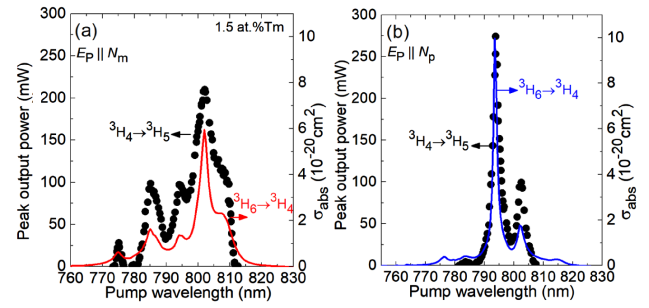
670 The higher slope efficiency for the laser operating on the
 671 ${}^3\text{H}_4 \rightarrow {}^3\text{H}_5$ transition is due to another energy-transfer process,
 672 namely ETU (see Section 4.E).

673 D. ${}^3\text{H}_4 \rightarrow {}^3\text{H}_5$ Transition: Effect of Pump Polarization

674 The strong anisotropy of the spectroscopic properties of
 675 Tm : KLu(WO₄)₂ allows one to select the pump polarization
 676 along different principal optical directions. In Fig. 11, we compare
 677 the performance of the same crystal (1.5 at. % Tm-doped)
 678 pumped with $\mathbf{E}_P \parallel N_p$ and $\mathbf{E}_P \parallel N_m$ polarizations. Note the
 679 difference in the corresponding pump wavelengths, 793.8 nm
 680 and 802.1 nm, respectively, corresponding to different local
 681 peaks in the absorption spectra. Physically, this difference arises
 682 from different polarization selection rules for light polarized
 683 along the C₂ symmetry axis ($\parallel N_p$) and for light polarizations
 684 lying in the mirror plane ($\perp C_2$, $\parallel N_m$) of the monoclinic
 685 KLu(WO₄)₂ crystal. Pumping in $\mathbf{E}_P \parallel N_p$ gives access to much
 686 higher peak absorption cross sections $\sigma_{\text{abs}} = 10.0 \times 10^{-20} \text{ cm}^2$
 687 while smaller absorption bandwidth $\Delta\lambda_{\text{abs}} = 1.6 \text{ nm}$, as compared
 688 to pumping in $\mathbf{E}_P \parallel N_m$ ($\sigma_{\text{abs}} = 5.95 \times 10^{-20} \text{ cm}^2$ and
 689 $\Delta\lambda_{\text{abs}} = 4.0 \text{ nm}$) [31].



674 **Fig. 11.** Effect of the pump polarization ($\mathbf{E}_P \parallel N_m$ and $\mathbf{E}_P \parallel N_p$) on
 675 ${}^3\text{H}_4 \rightarrow {}^3\text{H}_5$ laser performance; η , slope efficiency. (b) Laser emission
 676 spectra captured at $P_{\text{abs}} = 1.1 \text{ W}$ for 1.5 at. % Tm : KLu(WO₄)₂.
 677 Quasi-CW operation (duty cycle, 1:2). The laser polarization is
 678 $\mathbf{E} \parallel N_m$.



679 **Fig. 12.** Laser excitation spectra (output power versus pump
 680 wavelength) for the Tm laser operating on the ${}^3\text{H}_4 \rightarrow {}^3\text{H}_5$
 681 transition for pump polarization (a) $\mathbf{E}_P \parallel N_m$ and (b) $\mathbf{E}_P \parallel N_p$. The absorption
 682 cross sections, σ_{abs} , for the ${}^3\text{H}_6 \rightarrow {}^3\text{H}_4$ Tm³⁺ transition are shown for
 683 comparison. Quasi-CW operation (duty cycle, 1:2). $P_{\text{inc}} = 1.8 \text{ W}$. Tm
 684 doping, 1.5 at. %.

690 Slightly better laser performance was observed for pump-
 691 ing with $\mathbf{E}_P \parallel N_p$: the laser generated 0.42 W at $\sim 2290 \text{ nm}$
 692 with $\eta = 25.9\%$ and a laser threshold of $P_{\text{th}} = 0.30 \text{ W}$. For
 693 the second studied pump polarization, the laser threshold
 694 slightly increased to $P_{\text{th}} = 0.32 \text{ W}$, and the output dependence
 695 was more nonlinear above it. This led to lower output power
 696 (0.35 W) at $\sim 2292 \text{ nm}$. However, the slope efficiency was
 697 almost unchanged ($\eta = 24.7\%$). All the characteristics are
 698 specified for $T_{\text{OC}} = 1.3\%$. The pump absorption when pump-
 699 ing in $\mathbf{E}_P \parallel N_p$ was slightly higher. The total (double-pass)
 700 pump absorption at the threshold pump power $\eta_{\text{abs,L}(2\text{-pass})}$
 701 for $T_{\text{OC}} = 1.3\%$ was calculated to be 96.2% and 92.3% for
 702 $\mathbf{E}_P \parallel N_p$ and $\mathbf{E}_P \parallel N_m$, respectively.

703 In Fig. 12, we present the laser excitation spectra for the
 704 1.5 at. % Tm : KLu(WO₄)₂ pumped in two polarizations,
 705 $\mathbf{E}_P \parallel N_p$ and $\mathbf{E}_P \parallel N_m$, i.e., plots of the (peak) output power
 706 versus the pump wavelength λ_P . The incident pump power was
 707 fixed to $P_{\text{inc}} = 1.8 \text{ W}$, and it was weakly dependent (within a
 708 measurement error of $\pm 5\%$) on λ_P in the 770–820 nm spectral
 709 range. The coatings of the PM and OC exhibited flat spec-
 710 tral profiles at these wavelengths. Independent of the pump
 711 polarization, the laser polarization was naturally selected to be
 712 $\mathbf{E} \parallel N_m$. In Fig. 12, for comparison, we also show the polarized
 713 absorption cross section spectra for the ${}^3\text{H}_6 \rightarrow {}^3\text{H}_4$ Tm³⁺
 714 transition. For $\mathbf{E}_P \parallel N_p$, laser emission was observed when varying
 715 the pump wavelength in the 781.2–807.6 nm range and for
 716 $\mathbf{E}_P \parallel N_m$ –in the 773.1–812.7 nm range. The shape of the laser
 717 excitation spectra matched well that of the polarized absorption
 718 spectra.

719 E. ${}^3\text{H}_4 \rightarrow {}^3\text{H}_5$ Transition: Effect of the Doping 720 Concentration

721 A summary of the laser experiments on the ${}^3\text{H}_4 \rightarrow {}^3\text{H}_5$ Tm³⁺
 722 transition with the 0.5, 1.5, and 3.0 at. % Tm³⁺-doped crystals
 723 performed with polarized pump ($\mathbf{E}_P \parallel N_p$ and $\mathbf{E}_P \parallel N_m$) is
 724 presented in Table 2. The input-output dependences measured
 725 using the same output coupling ($T_{\text{OC}} = 1.3\%$) and
 726 pump polarization ($\mathbf{E}_P \parallel N_p$) are compared in Fig. 13(a). With
 727 increasing the Tm doping concentration, the slope efficiency
 728 of the laser η greatly increased from 10.7% (0.5 at. % Tm) to
 729 69.2% (3.0 at. % Tm), so that the maximum slope efficiency

Table 2. Output Characteristics^a of Thulium Lasers at ~2.3 μm

Tm, at. %	λ_p , nm	P_{out} , W	η , %	P_{th} , W	λ_L , nm	η_{opt} , %
0.5	793.8 (N_p)	0.17	10.7	0.28	2290–2293	6.9
1.5	793.8 (N_p)	0.42	25.9	0.30	2288–2290	17.6
	802.1 (N_m)	0.35	24.7	0.32	2291–2292	14.4
3.0	793.8 (N_p)	1.12	69.2	0.45	2218–2223, 2290–2294	44.4
	802.1 (N_m)	1.02	67.7	0.44	2214–2219, 2289–2293	40.5

^a λ_p , pump wavelength (polarization given in brackets); P_{out} , peak output power; P_{th} , laser threshold; η , slope efficiency versus P_{abs} ; λ_L , laser wavelength; η_{opt} , optical-to-optical efficiency. $T_{OC} = 1.3\%$.

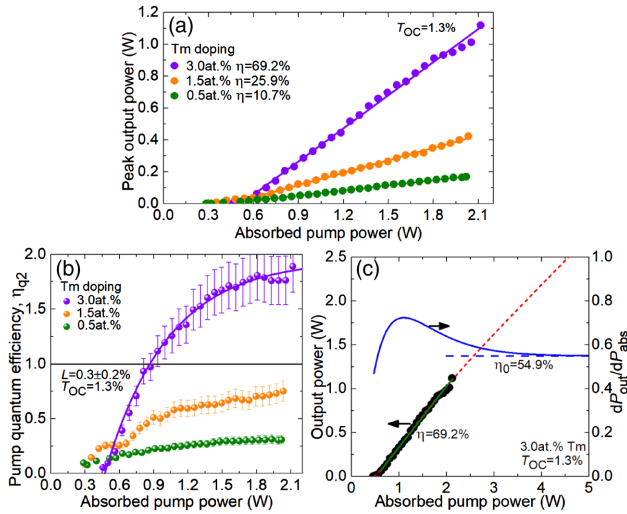


Fig. 13. Effect of doping concentration on the performance of Tm lasers operating on the ${}^3H_4 \rightarrow {}^3H_5$ transition: (a) input-output dependences, η , slope efficiency. (b) Pump quantum efficiency η_{q2} : symbols, data calculated using Eq. (6); violet curve, empirical fit. (c) Output power and slope efficiency for 3 at. % Tm-doped crystal: circles, experimental data on the output power; green line, their linear fit yielding experimental η ; red dashed curve, extrapolated output power calculated using Eq. (6); blue curve, dP_{out}/dP_{abs} , Eq. (7); dashed blue line, the intrinsic slope efficiency η_0 , Eq. (8). $T_{OC} = 1.3\%$; $\lambda_p = 793.8$ nm; pump polarization, $E_p || N_p$. Quasi-CW operation (duty cycle, 1:2).

well exceeded the S limit, $\eta_{St,L} = 35.8\%$. Let us discuss this behavior.

Recently, we developed a model describing Tm lasers operating on the ${}^3H_4 \rightarrow {}^3H_5$ transition [25]. It is based on accounting for two key energy-transfer processes affecting the population of the upper laser level (3H_4), namely the CR, ${}^3H_4(Tm_1) + {}^3H_6(Tm_2) \rightarrow {}^3F_4(Tm_1) + {}^3F_4(Tm_2)$, and the reverse process of ETU, ${}^3F_4(Tm_1) + {}^3F_4(Tm_2) \rightarrow {}^3H_6(Tm_1) + {}^3H_4(Tm_2)$. The CR depopulates the upper laser level while the ETU brings the ions back using the metastable 3F_4 state as a “reservoir” of electronic excitations. Thus, contrary to the ~ 1.9 μm laser transition, ETU plays a positive role for the ~ 2.3 μm lasers, while the CR is a detrimental effect. The pump quantum efficiency η_{q2} , defined as the number of electronic excitations to the 3H_4 level per number of absorbed pump photons at ~ 0.8 μm, can thus vary in the range of $0 < \eta_{q2} < 2$,

where values below unity are governed by CR (assuming no ETU) and values above unity indicate efficient ETU.

The pump quantum efficiency η_{q2} can be evaluated from the input-output dependence according to the following analytical equation [25]:

$$P_{out} = \frac{h\nu_L w_L^2}{h\nu_P w_P^2} \frac{T_{OC}}{T_{OC} + L} \eta_{q2} P_{abs} - \frac{T_{OC} h\nu_L \pi w_L^2}{2\sigma_{SE}^L \tau_{30}}. \quad (6)$$

where P_{out} and P_{abs} are the output laser power and the absorbed pump power, respectively, h is the Planck constant, and ν_L and ν_P are the laser and pump frequencies, respectively. The results on η_{q2} obtained using a round trip loss $L = 0.3 \pm 0.2\%$ are shown in Fig. 13(c). The L value was taken to be slightly smaller than that estimated in Section 4.C because of the longer laser wavelength and the lack of reabsorption. For all the studied Tm concentrations, the pump quantum efficiency gradually increases with the pump power, and this dependence saturates well above the laser threshold. This can be explained as follows. In laser operation on the ${}^3H_4 \rightarrow {}^3H_5$ transition, the inversion rate is clamped by the condition “gain equals losses.” However, the absolute population density of the 3F_4 state is not fixed and grows with the pump power. Indeed, direct measurements of the pump absorption under lasing conditions in ~ 2.3 μm Tm lasers indicate ground-state bleaching above threshold [25]. Thus, the rate of the ETU process, which is proportional to the squared population density of the 3F_4 state, increases with the pump power. This may be partially responsible for the nonlinear input-output dependences of the laser (another reason is the spatially non-uniform gain). At high pump powers well above the laser threshold, η_{q2} reaches a pump-independent value determined by a counteraction of CR and ETU leading to a linear output dependence.

Another observation is that for small Tm doping levels (0.5–1.5 at. %), η_{q2} is below unity. For the medium doping of 3 at. % Tm, it approaches 1.8 ± 0.1 , which explains the observed high laser efficiency. Moreover, with increasing Tm concentration, the maximum pump quantum efficiency gradually increases. It seems that the positive effect of ETU on the performance of ~ 2.3 μm lasers based on Tm : KLu(WO₄)₂ crystals is enhanced with the Tm doping concentration faster than the negative effect of CR.

Let us discuss the definition of the slope efficiency of a Tm laser operating on the ${}^3H_4 \rightarrow {}^3H_5$ transition. By definition, $\eta = dP_{out}/dP_{abs}$. If the input-output dependence is linear within a certain range of pump powers, this will lead to a constant η value. By applying this definition to Eq. (6), we achieve

$$\frac{dP_{out}}{dP_{abs}} = \eta_{St,L} \eta_{mode} \eta_{OC} \left(\eta_{q2}(P_{abs}) + \frac{d\eta_{q2}}{dP_{abs}} P_{abs} \right). \quad (7)$$

Here, η_{mode} is the mode overlap efficiency, and η_{OC} is the output coupling efficiency. As the pump quantum efficiency for the ${}^3H_4 \rightarrow {}^3H_5$ transition η_{q2} is pump-dependent, cf. Fig. 13(b), dP_{out}/dP_{abs} is not constant. For high pump powers well exceeding the laser threshold, the power dependence of η_{q2} is saturated ($\eta_{q2} \rightarrow \eta_{q2,0}$), so that

$$\eta_0 = \left. \frac{dP_{out}}{dP_{abs}} \right|_{P_{abs} \gg P_{th}} = \eta_{St,L} \eta_{mode} \eta_{OC} \eta_{q2,0}. \quad (8)$$

746
747
748
749
750
751
752
753
754
755
756
757
758
759
760
761
762
763
764
765
766
767
768
769
770
771
772
773
774
775
776
777
778
779
780
781
782
783
784
785
786
787
788
789
790
791
792
793
794
795

Table 3. Summary^a of Laser-Pumped Thulium Lasers Operating on the $^3\text{H}_4 \rightarrow ^3\text{H}_5$ Transition Reported So Far

Crystal ^b	Tm, at. %	$h\nu_{ph}$, cm^{-1}	σ_{SE} , 10^{-20} cm^2	τ_{30} , ms	λ_P , nm	P_{th} , W	P_{out} , W	η , %	λ_L , μm	M^2	Polariz.	Ref.
Tm:LiYF ₄	3.5	446	0.57	2.30	780	0.39	0.73 ^c _q ^{CW}	47.3	2.31	—	$E c(\pi)$	[25]
Tm:KY ₃ F ₁₀	5.0	495	0.34	1.90	773	0.82	0.84 ^{CW}	53.8	2.34	2.1–2.3	unpolarized	[26]
Tm:BaY ₂ F ₈	3.0	421	0.49 [57]	1.10	779	~0.12	0.10 ^{CW}	12	2.29	1.1	$E X$	[55]
Tm:YAlO ₃	1.8	552	0.78	0.70	776	0.41	0.96 ^{CW}	61.8	2.27	—	$E b$	[56]
Tm:Y ₃ Al ₅ O ₁₂	3.2	857	0.35	0.79	781	0.86	1.07 ^{CW}	46.3	2.19, 2.32	3.4	unpolarized	[29]
Tm:KLu(WO ₄) ₂	3.0	907	1.78	0.24	793	0.45	1.12 ^{CW}	69.2	2.22, 2.29	2.2–2.6	$E N_m$	^c

^a $h\nu_{ph}$, highest phonon energy of the host matrix; σ_{SE} , peak stimulated-emission cross section at $\sim 2.3 \mu\text{m}$; τ_{30} , intrinsic lifetime of the $^3\text{H}_4$ state; λ_P , pump wavelength; P_{th} , laser threshold; P_{out} , output power; η , slope efficiency; λ_L , laser wavelength.

^bBest results selected from multiple publications on the same crystal.

^cThis work.

This equation gives a well-known definition of the laser slope efficiency.

In Fig. 13(c), we extrapolated the output power of the Tm laser using Eq. (6) and fitted the data on the pump quantum efficiency using an empirical formula $\eta_{q2} = \eta_{q2,0} * \exp[-(P_{abs} - P_{th})/P_0]$, where P_0 is a free parameter, as shown in Fig. 13(b). The result of this extrapolation is shown by the red dashed curve. Accordingly, we determine dP_{out}/dP_{abs} using Eq. (7), as shown by the blue solid curve. dP_{out}/dP_{abs} first increases above the laser threshold and then decreases asymptotically reaching the value of η_0 , which is determined by Eq. (8). For the considered laser, $\eta_0 = 54.9 \pm 3\%$. Note that this value is almost not sensitive to the round trip passive loss used for the calculations. η_0 can be further improved under the condition of η_{mode} and η_{OC} both approaching unity (excellent mode-matching and very low round trip intracavity losses), so that

$$\eta_0 \leq 2\eta_{St,L}. \quad (9)$$

This equation represents an upper limit for the slope efficiency of a Tm laser operating on the $^3\text{H}_4 \rightarrow ^3\text{H}_5$ transition and represents an ideal two-for-one pump process.

F. $^3\text{H}_4 \rightarrow ^3\text{H}_5$ Transition: Comparison with Other Hosts

So far, CW laser operation on the $^3\text{H}_4 \rightarrow ^3\text{H}_5$ transition has been achieved in very few Tm³⁺-doped fluoride (LiYF₄ [25], KY₃F₁₀ [26,54], BaY₂F₈ [55]) and oxide (Y₃Al₅O₁₂ [29], YAlO₃ [30,56]) crystals. Among these results, we selected only those relying on laser-pumping at $\sim 0.8 \mu\text{m}$ (to the $^3\text{H}_4$ state, conventional pump scheme). For this, typically, a Ti:sapphire laser has been used as a pump source. The best results selected from publications on the topic are summarized in Table 3 highlighting the Tm doping level, the maximum phonon frequency of the host matrix $h\nu_{ph}$, the spectroscopic properties at the laser wavelength, and the CW laser performance.

The Tm:KLu(WO₄)₂ crystal features the highest maximum phonon frequency (907 cm^{-1}) among the crystals intended for $\sim 2.3 \mu\text{m}$ Tm lasers. It also provides the highest SE cross section for the $^3\text{H}_4 \rightarrow ^3\text{H}_5$ transition in polarized light, owing to the strong polarization-anisotropy of spectroscopic properties of this monoclinic crystal, and relatively short radiative lifetime of the upper laser level. Moreover, we report on the highest output power and slope efficiency ever achieved from a laser-pumped

$\sim 2.3 \mu\text{m}$ Tm laser using a 3.0 at. % Tm:KLu(WO₄)₂ crystal. The slope efficiency (69.2%) almost approaches the limit set by 2 times the S efficiency, highlighting the very efficient ETU in this material.

An important parameter of the laser host crystal to be included in the comparison is the thermal conductivity κ . Its mean value for KLu(WO₄)₂ is $\langle \kappa \rangle = 3.12 \text{ Wm}^{-1} \text{ K}^{-1}$ [58]. This value is lower than for other crystals considered in Table 3. Thus, thermal management of Tm lasers based on this crystalline host is very important.

Note that for pumping in the same absorption band of Tm³⁺ ($^3\text{H}_6 \rightarrow ^3\text{H}_4$), AlGaAs laser diodes can be also used [59,60]. The main issues for diode-pumped $\sim 2.3 \mu\text{m}$ Tm lasers (as compared to those pumped by high-brightness sources such as bulk or fiber lasers) are the following: (i) higher laser thresholds, (ii) the key role of optimized mode-matching between the pump and laser radiation preventing the appearance of higher-order modes and colasing at $\sim 1.9 \mu\text{m}$, and (iii) more serious thermal effects in the active element.

5. CONCLUSION

To conclude, solid-state lasers based on Tm³⁺-doped materials and operating on the $^3\text{H}_4 \rightarrow ^3\text{H}_5$ transition are excellent candidates for highly efficient coherent light sources in the short-wave infrared spectral range and, in particular, at $\sim 2.3 \mu\text{m}$. Contrary to well-established models, they are rather tolerant to such key parameters of the gain media as their phonon spectra and Tm doping levels. This is due to the relatively complex physical nature of the $^3\text{H}_4 \rightarrow ^3\text{H}_5$ laser scheme affected by both CR and ETU between neighboring Tm³⁺ ions. We prove that highly efficient lasing at $\sim 2.3 \mu\text{m}$ (with a slope efficiency exceeding the S limit) can be achieved even in high-phonon energy Tm³⁺-doped crystals at moderate doping levels leading to a notable self-quenching of the upper laser level by CR. An evidence of a two-for-one pump process associated with the ETU refilling the upper laser level and probably with the gain at the vibronic sideband of the $^3\text{F}_4 \rightarrow ^3\text{H}_6$ transition has been provided. A compact Tm:KLu(WO₄)₂ laser generated a watt-level output at ~ 2.22 and $2.29 \mu\text{m}$ (multi-color emission) with a slope efficiency of 69.2%—a record-high for this type of lasers. Thus, it can be expected that other Tm³⁺-doped oxide crystals may be also of practical importance for $\sim 2.3 \mu\text{m}$ lasers by providing better power scaling or other laser wavelengths.

We also extend the understanding of the physical nature of emission at wavelengths lying between the ${}^3\text{H}_4 \rightarrow {}^3\text{H}_5$ and ${}^3\text{F}_4 \rightarrow {}^3\text{H}_6$ electronic transitions. First, we determined the SE cross sections for Tm^{3+} ions in $\text{KLu}(\text{WO}_4)_2$, which reached $1.78 \times 10^{-20} \text{ cm}^2$ at 2289 nm for the former transition representing the highest value among all the Tm^{3+} -doped materials (crystals, ceramics, and glasses) studied so far. We were able to assign multiple observed laser lines lying between 2.14 and 2.30 μm to electronic transitions occurring between the Stark sub-levels of the ${}^3\text{H}_4$ and ${}^3\text{H}_5$ multiplets. We also showed that vibronic transitions bridge the gap between the ${}^3\text{H}_4 \rightarrow {}^3\text{H}_5$ and ${}^3\text{F}_4 \rightarrow {}^3\text{H}_6$ electronic transitions leading to a non-vanishing SE cross section and, potentially, optical gain within this spectral range. Based on these studies, we were able to explain previous findings on vibronic Tm lasers. Our results indicate that Tm^{3+} -doped monoclinic double tungstate crystals may provide a continuously tunable laser emission over an ultra-broad spectral range of about 1.7–2.5 μm .

We highlight the suitability of Tm^{3+} -doped monoclinic double tungstates for fs ML lasers at $\sim 2.3 \mu\text{m}$ based on their broad emission spectra (bandwidth exceeding 30 nm, not affected by the inversion rate). Another relevant conclusion of our work is the possible contribution of ${}^3\text{H}_4 \rightarrow {}^3\text{H}_5$ and ${}^3\text{F}_4 \rightarrow {}^3\text{H}_6$ related vibronic emissions to the very broad emission spectra of ML thulium lasers extending beyond 2 μm , observed so far in several crystals [61,62]. This should be clarified further, e.g., by comparing the resonant Raman and vibronic gain in such materials.

Further power scaling of monoclinic double tungstate-based $\sim 2.3 \mu\text{m}$ Tm lasers can be realized in several ways, i.e., (i) by using other pump sources, such as laser diodes at $\sim 0.8 \mu\text{m}$ (for the conventional pump scheme), Er Raman fiber lasers emitting at $\sim 1.6 \mu\text{m}$ (in-band pumping [63]) or Yb fiber lasers at $\sim 1 \mu\text{m}$ (upconversion pumping [64], which would require the measurements of the excited-state absorption spectra); or (ii) by using short highly doped samples (5–15 at. % Tm) for better pump absorption, pump and laser mode overlap, and high slope efficiency. The latter approach will require a rate-equation modeling of the Tm^{3+} system involving the ETU and energy-migrations rate constants, which are still unknown for monoclinic double tungstates. The power scaling will raise the question of the fractional heat loading under laser operation on the ${}^3\text{H}_4 \rightarrow {}^3\text{H}_5$ transition. Finally, as Tm^{3+} -doped monoclinic double tungstates provide a positive thermal lens for certain crystal cuts, microchip $\sim 2.3 \mu\text{m}$ lasers should be feasible.

Funding. French Agence Nationale de la Recherche (ANR) (LabEx EMC3 (ANR-10-LABX-09-01), SPLENDID2 (ANR-19-CE08-0028)); European Community (European project “NOVAMAT”); Spanish Government, MINECO (MAT2016-75716-C2-1-R (AEI/FEDER/UE), PID2019-108543RB-I00); Generalitat de Catalunya (2017SGR755).

Disclosures. The authors declare no conflicts of interest.

REFERENCES

1. F. J. McAleavey, J. O’Gorman, J. F. Donegan, B. D. MacCraith, J. Hegarty, and G. Mazé, “Narrow linewidth, tunable Tm^{3+} -doped fluoride fiber laser for optical-based hydrocarbon gas sensing,” *IEEE J. Sel. Top. Quantum Electron.* **3**, 1103–1111 (1997).

2. A. Garnache, A. Liu, L. Cerutti, and A. Campargue, “Intracavity laser absorption spectroscopy with a vertical external cavity surface emitting laser at 2.3 μm : application to water and carbon dioxide,” *Chem. Phys. Lett.* **416**, 22–27 (2005).
3. M. E. Webber, J. Wang, S. T. Sanders, D. S. Baer, and R. K. Hanson, “*In situ* combustion measurements of CO, CO₂, H₂O and temperature using diode laser absorption sensors,” *Proc. Combust. Inst.* **28**, 407–413 (2000).
4. S. T. Fard, W. Hofmann, P. T. Fard, G. Bohm, M. Ortsiefer, E. Kwok, M.-C. Amann, and L. Chrostowski, “Optical absorption glucose measurements using 2.3 μm vertical-cavity semiconductor lasers,” *IEEE Photon. Technol. Lett.* **20**, 930–932 (2008).
5. V. Petrov, “Frequency down-conversion of solid-state laser sources to the mid-infrared spectral range using non-oxide nonlinear crystals,” *Prog. Quantum Electron.* **42**, 1–106 (2015).
6. S. Mirov, V. Fedorov, I. Moskalev, D. Martyshkin, and C. Kim, “Progress in Cr²⁺ and Fe²⁺ doped mid-IR laser materials,” *Laser Photon. Rev.* **4**, 21–41 (2010).
7. I. T. Sorokina, E. Sorokin, S. Mirov, V. Fedorov, V. Badikov, V. Panyutin, A. Di Lieto, and M. Tonelli, “Continuous-wave tunable Cr²⁺:ZnS laser,” *Appl. Phys. B* **74**, 607–611 (2002).
8. I. T. Sorokina, “Cr²⁺-doped II-VI materials for lasers and nonlinear optics,” *Opt. Mater.* **26**, 395–412 (2004).
9. N. Tolstik, E. Sorokin, and I. T. Sorokina, “Graphene mode-locked Cr:ZnS laser with 41 fs pulse duration,” *Opt. Express* **22**, 5564–5571 (2014).
10. T. J. Carrig, G. J. Wagner, A. Sennaroglu, J. Y. Jeong, and C. R. Pollock, “Mode-locked Cr²⁺:ZnSe laser,” *Opt. Lett.* **25**, 168–170 (2000).
11. E. Geerlings, M. Rattunde, J. Schmitz, G. Kaufel, H. Zappe, and J. Wagner, “Widely tunable GaSb-based external cavity diode laser emitting around 2.3 μm ,” *IEEE Photon. Technol. Lett.* **18**, 1913–1915 (2006).
12. G. Boehm, A. Bachmann, J. Roskopf, M. Ortsiefer, J. Chen, A. Hangauer, R. Meyer, R. Strzoda, and M.-C. Amann, “Comparison of InP- and GaSb-based VCSELs emitting at 2.3 μm suitable for carbon monoxide detection,” *J. Cryst. Growth* **323**, 442–445 (2011).
13. L. Shterengas, G. L. Belenky, A. Gourevitch, D. Donetsky, J. G. Kim, R. U. Martinelli, and D. Westerfeld, “High-power 2.3- μm GaSb-based linear laser array,” *IEEE Photon. Technol. Lett.* **16**, 2218–2220 (2004).
14. Ò. Silvestre, M. C. Pujol, M. Rico, F. Güell, M. Aguiló, and F. Díaz, “Thulium doped monoclinic $\text{KLu}(\text{WO}_4)_2$ single crystals: growth and spectroscopy,” *Appl. Phys. B* **87**, 707–716 (2007).
15. J. Caird, L. DeShazer, and J. Nella, “Characteristics of room-temperature 2.3- μm laser emission from Tm^{3+} in YAG and YAlO_3 ,” *IEEE J. Quantum Electron.* **11**, 874–881 (1975).
16. R. Allen and L. Esterowitz, “CW diode pumped 2.3 μm fiber laser,” *Appl. Phys. Lett.* **55**, 721–722 (1989).
17. R. C. Stoneman and L. Esterowitz, “Efficient, broadly tunable, laser-pumped $\text{Tm}:\text{YAG}$ and $\text{Tm}:\text{YSGG}$ cw lasers,” *Opt. Lett.* **15**, 486–488 (1990).
18. K. van Dalen, S. Aravazhi, C. Grivas, S. M. García-Blanco, and M. Pollnau, “Thulium channel waveguide laser with 1.6 W of output power and $\sim 80\%$ slope efficiency,” *Opt. Lett.* **39**, 4380–4383 (2014).
19. R. Souillard, M. Salhi, G. Brasse, P. Loiko, J.-L. Doualan, L. Guillemot, A. Braud, A. Tyazhev, A. Hideur, and P. Camy, “Laser operation of highly-doped $\text{Tm}:\text{LiYF}_4$ epitaxies: towards thin-disk lasers,” *Opt. Express* **27**, 9287–9301 (2019).
20. I. Yorulmaz and A. Sennaroglu, “Low-threshold diode-pumped 2.3- μm $\text{Tm}^{3+}:\text{YLF}$ lasers,” *IEEE J. Sel. Top. Quantum Electron.* **24**, 2791409 (2018).
21. J. F. Pinto, L. Esterowitz, and G. H. Rosenblatt, “ $\text{Tm}^{3+}:\text{YLF}$ laser continuously tunable between 2.20 and 2.46 μm ,” *Opt. Lett.* **19**, 883–885 (1994).
22. R. M. El-Agmy and N. M. Al-Hosiny, “2.31 μm laser under up-conversion pumping at 1.064 μm in $\text{Tm}^{3+}:\text{ZBLAN}$ fibre lasers,” *Electron. Lett.* **46**, 936–937 (2010).
23. R. Souillard, A. Tyazhev, J.-L. Doualan, A. Braud, A. Hideur, M. Laroche, B. Xu, and P. Camy, “2.3 μm $\text{Tm}^{3+}:\text{YLF}$ mode-locked laser,” *Opt. Lett.* **42**, 3534–3536 (2017).

- 1005 24. F. Canbaz, I. Yorulmaz, and A. Sennaroglu, "Kerr-lens mode-locked
1006 2.3- μm Tm^{3+} :YLF laser as a source of femtosecond pulses in the
1007 mid-infrared," *Opt. Lett.* **42**, 3964–3967 (2017).
- 1008 25. P. Loiko, R. Souillard, L. Guillemot, G. Brasse, J.-L. Doualan, A. Braud,
1009 A. Tyazhev, A. Hideur, B. Guichardaz, F. Druon, and P. Camy,
1010 "Efficient $\text{Tm}:\text{LiYF}_4$ lasers at ~ 2.3 μm : effect of energy-transfer
1011 upconversion," *IEEE J. Quantum Electron.* **55**, 2943477 (2019).
- 1012 26. L. Guillemot, P. Loiko, R. Souillard, A. Braud, J.-L. Doualan, A. Hideur,
1013 and P. Camy, "Close look on cubic $\text{Tm}:\text{KY}_3\text{F}_{10}$ crystal for highly effi-
1014 cient lasing on the ${}^3\text{H}_4 \rightarrow {}^3\text{H}_5$ transition," *Opt. Express* **28**, 3451–3463
1015 (2020).
- 1016 27. L. Guillemot, P. Loiko, R. Souillard, A. Braud, J.-L. Doualan, A. Hideur,
1017 R. Moncorgé, and P. Camy, "Thulium laser at ~ 2.3 μm based on
1018 upconversion pumping," *Opt. Lett.* **44**, 4071–4074 (2019).
- 1019 28. Y. Morova, M. Tonelli, V. Petrov, and A. Sennaroglu, "Upconversion
1020 pumping of a 2.3 μm $\text{Tm}^{3+}:\text{KY}_3\text{F}_{10}$ laser with a 1064 nm ytterbium
1021 fiber laser," *Opt. Lett.* **45**, 931–934 (2020).
- 1022 29. L. Guillemot, P. Loiko, E. Kifle, J.-L. Doualan, A. Braud, F. Starecki,
1023 T. Georges, J. Rouvillain, A. Hideur, and P. Camy, "Watt-level mid-
1024 infrared continuous-wave $\text{Tm}:\text{YAG}$ laser operating on the ${}^3\text{H}_4 \rightarrow {}^3\text{H}_5$
1025 transition," *Opt. Mater.* **101**, 109745 (2020).
- 1026 30. L. Guillemot, P. Loiko, A. Braud, J.-L. Doualan, A. Hideur, M. Koselja,
1027 R. Moncorgé, and P. Camy, "Continuous-wave $\text{Tm}:\text{YAlO}_3$ laser at
1028 ~ 2.3 μm ," *Opt. Lett.* **44**, 5077–5080 (2019).
- 1029 31. V. Petrov, M. C. Pujol, X. Mateos, Ö. Silvestre, S. Rivier, M. Aguiló,
1030 R. M. Solé, J. Liu, U. Griebner, and F. Díaz, "Growth and properties
1031 of $\text{KLu}(\text{WO}_4)_2$, and novel ytterbium and thulium lasers based on this
1032 monoclinic crystalline host," *Laser Photon. Rev.* **1**, 179–212 (2007).
- 1033 32. J. M. Serres, X. Mateos, P. Loiko, K. Yumashev, N. Kulshov,
1034 V. Petrov, U. Griebner, M. Aguiló, and F. Díaz, "Diode-pumped
1035 microchip $\text{Tm}:\text{KLu}(\text{WO}_4)_2$ laser with more than 3 W of output power,"
1036 *Opt. Lett.* **39**, 4247–4250 (2014).
- 1037 33. P. Loiko, J. M. Serres, X. Mateos, K. Yumashev, A. Yasukevich,
1038 V. Petrov, U. Griebner, M. Aguiló, and F. Díaz, "Subnanosecond
1039 $\text{Tm}:\text{KLuW}$ microchip laser Q-switched by a $\text{Cr}:\text{ZnS}$ saturable
1040 absorber," *Opt. Lett.* **40**, 5220–5223 (2015).
- 1041 34. A. Schmidt, S. Y. Choi, D. I. Yeom, F. Rotermund, X. Mateos, M.
1042 Segura, F. Díaz, V. Petrov, and U. Griebner, "Femtosecond pulses
1043 near 2 μm from a $\text{Tm}:\text{KLuW}$ laser mode-locked by a single-walled
1044 carbon nanotube saturable absorber," *Appl. Phys. Express* **5**,
1045 092704 (2012).
- 1046 35. A. A. Kaminskii, K. Ueda, H. E. Eichler, J. Findeisen, S. N. Bagayev,
1047 F. A. Kuznetsov, A. A. Pavlyuk, G. Boulon, and F. Bourgeois,
1048 "Monoclinic tungstates $\text{KdY}(\text{WO}_4)_2$ and $\text{KLu}(\text{WO}_4)_2$ —new $\chi^{(3)}$ -active
1049 crystals for laser Raman shifters," *Jpn. J. Appl. Phys.* **37**, L923–L926
1050 (1998).
- 1051 36. H. Scheife, G. Huber, E. Heumann, S. Bär, and E. Osic, "Advances in
1052 up-conversion lasers based on Er^{3+} and Pr^{3+} ," *Opt. Mater.* **26**, 365–
1053 374 (2004).
- 1054 37. P. Loiko, P. Segonds, P. L. Inácio, A. Peña, J. Debray, D. Rytz, V.
1055 Filippon, K. Yumashev, M. C. Pujol, X. Mateos, M. Aguiló, F. Díaz, M.
1056 Eichhorn, and B. Boulanger, "Refined orientation of the optical axes
1057 as a function of wavelength in three monoclinic double tungstate
1058 crystals $\text{KRE}(\text{WO}_4)_2$ ($\text{RE} = \text{Gd}, \text{Y}$ or Lu)," *Opt. Mater. Express* **6**,
1059 2984–2990 (2016).
- 1060 38. B. Aull and H. Jenssen, "Vibronic interactions in $\text{Nd}:\text{YAG}$ result-
1061 ing in nonreciprocity of absorption and stimulated emission cross
1062 sections," *IEEE J. Quantum Electron.* **18**, 925–930 (1982).
- 1063 39. A. Ellens, S. Schenker, A. Meijerink, and G. Blasse, "Vibronic transi-
1064 tions of Tm^{3+} in various lattices," *J. Lumin.* **69**, 1–15 (1996).
- 1065 40. W. F. Krupke, "Optical absorption and fluorescence intensities in sev-
1066 eral rare-earth-doped Y_2O_3 and LaF_3 single crystals," *Phys. Rev.* **145**,
1067 325–337 (1966).
- 1068 41. F. Auzel, "Multiphonon-assisted anti-Stokes and Stokes fluores-
1069 cence of triply ionized rare-earth ions," *Phys. Rev. B* **13**, 2809–2817
1070 (1976).
- 1071 42. A. Braud, S. Girard, J. L. Doualan, and R. Moncorgé, "Spectroscopy
1072 and fluorescence dynamics of (Tm^{3+} , Tb^{3+}) and (Tm^{3+} , Eu^{3+}) doped
1073 LiYF_4 single crystals for 1.5- μm laser operation," *IEEE J. Quantum*
1074 *Electron.* **34**, 2246–2255 (1988).
- 1075 43. X. Mateos, P. Loiko, J. M. Serres, K. Yumashev, U. Griebner, V.
1076 Petrov, M. Aguiló, and F. Díaz, "Efficient micro-lasers based on highly
doped monoclinic double tungstates," *IEEE J. Quantum Electron.* **53**,
2681626 (2017).
- 1077 44. P. Loiko, X. Mateos, S. Y. Choi, F. Rotermund, J. M. Serres, M. Aguiló,
1078 F. Díaz, K. Yumashev, U. Griebner, and V. Petrov, "Vibronic thulium
1079 laser at 2131 nm Q-switched by single-walled carbon nanotubes," *J.*
1080 *Opt. Soc. Am. B.* **33**, D19–D27 (2016).
- 1081 45. M. J. Weber, "Radiative and multiphonon relaxation of rare-earth ions
1082 in Y_2O_3 ," *Phys. Rev.* **171**, 283–291 (1968).
- 1083 46. C. B. Layne, W. H. Lowdermilk, and M. J. Weber, "Multiphonon relax-
1084 ation of rare-earth ions in oxide glasses," *Phys. Rev. B* **16**, 10–20
1085 (1977).
- 1086 47. J. M. de Mendivil, G. Lifante, M. C. Pujol, M. Aguiló, F. Díaz, and E.
1087 Cantelar, "Judd–Ofelt analysis and transition probabilities of Er^{3+}
1088 doped $\text{KY}_{1-x-y}\text{Gd}_x\text{Lu}_y(\text{WO}_4)_2$ crystals," *J. Lumin.* **165**, 153–158
1089 (2015).
- 1090 48. M. C. Pujol, M. Rico, C. Zaldo, R. Solé, V. Nikolov, X. Solans, M.
1091 Aguiló, and F. Díaz, "Crystalline structure and optical spectroscopy of
1092 Er^{3+} -doped $\text{KGd}(\text{WO}_4)_2$ single crystals," *Appl. Phys. B* **68**, 187–197
1093 (1999).
- 1094 49. M. C. Pujol, J. Massons, M. Aguiló, F. Díaz, M. Rico, and C. Zaldo,
1095 "Emission cross sections and spectroscopy of Ho^{3+} laser channels
1096 in $\text{KGd}(\text{WO}_4)_2$ single crystal," *IEEE J. Quantum Electron.* **38**, 93–100
1097 (2002).
- 1098 50. A. A. Demidovich, A. N. Kuzmin, N. K. Nikeenko, A. N. Titov, M. Mond,
1099 and S. Kueck, "Optical characterization of $\text{Yb}, \text{Tm}:\text{KYW}$ crystal con-
1100 cerning laser application," *J. Alloys Compd.* **341**, 124–129 (2002).
- 1101 51. F. Güell, X. Mateos, J. Gavalda, R. Sole, M. Aguiló, F. Díaz, and J.
1102 Massons, "Blue luminescence in Tm^{3+} -doped $\text{KGd}(\text{WO}_4)_2$ single
1103 crystals," *J. Lumin.* **106**, 109–114 (2004).
- 1104 52. P. Loiko and M. Pollnau, "Stochastic model of energy-transfer proc-
1105 esses among rare-earth ions. Example of $\text{Al}_2\text{O}_3:\text{Tm}^{3+}$," *J. Phys.*
1106 *Chem. C* **120**, 26480–26489 (2016).
- 1107 53. J. A. Caird, S. A. Payne, P. R. Staber, A. J. Ramponi, L. L.
1108 Chase, and W. F. Krupke, "Quantum electronic properties of the
1109 $\text{Na}_3\text{Ga}_2\text{Li}_3\text{F}_{12}:\text{Cr}^{3+}$ laser," *IEEE J. Quantum Electron.* **24**, 1077–1099
1110 (1988).
- 1111 54. A. Muti, M. Tonelli, V. Petrov, and A. Sennaroglu, "Continuous-wave
1112 mid-infrared laser operation of $\text{Tm}^{3+}:\text{KY}_3\text{F}_{10}$ at 2.3 μm ," *Opt. Lett.*
1113 **44**, 3242–3245 (2019).
- 1114 55. A. Muti, I. Baylam, M. Tonelli, and A. Sennaroglu, "Tunable
1115 continuous-wave laser operation of $\text{Tm}^{3+}:\text{BaY}_2\text{F}_8$ near 2.3 μm ,"
1116 *Opt. Lett.* **45**, 4104–4107 (2020).
- 1117 56. L. Guillemot, P. Loiko, E. Kifle, A. Braud, J.-L. Doualan, A. Hideur, M.
1118 Koselja, R. Moncorgé, and P. Camy, "Spectroscopy and laser opera-
1119 tion of $\text{Tm}^{3+}:\text{YAlO}_3$ crystal on the ${}^3\text{H}_4 \rightarrow {}^3\text{H}_5$ transition," *Proc. SPIE*
1120 **11357**, 113570H (2020).
- 1121 57. P. Loiko, J. L. Doualan, L. Guillemot, R. Moncorgé, F. Starecki, A.
1122 Benayad, E. Dunina, A. Kornienko, L. Fomicheva, A. Braud, and P.
1123 Camy, "Emission properties of Tm^{3+} -doped CaF_2 , KY_3F_{10} , LiYF_4 ,
1124 LiLuF_4 and BaY_2F_8 crystals at 1.5 μm and 2.3 μm ," *J. Lumin.* **225**,
1125 117279 (2020).
- 1126 58. Ö. Silvestre, J. Grau, M. C. Pujol, J. Massons, M. Aguiló, F. Díaz, M. T.
1127 Borowiec, A. Szewczyk, M. U. Gutowska, M. Massot, A. Salazar, and
1128 V. Petrov, "Thermal properties of monoclinic $\text{KLu}(\text{WO}_4)_2$ as a promis-
1129 ing solid state laser host," *Opt. Express* **16**, 5022–5034 (2008).
- 1130 59. S. Wang, H. Huang, H. Chen, X. Liu, S. Liu, J. Xu, and D. Shen, "High
1131 efficiency nanosecond passively Q-switched 2.3 μm $\text{Tm}:\text{YLF}$ laser
1132 using a ReSe_2 -based saturable output coupler," *OSA Continuum* **2**,
1133 1676–1682 (2019).
- 1134 60. E. Kifle, P. Loiko, L. Guillemot, J.-L. Doualan, F. Starecki, A. Braud,
1135 T. Georges, J. Rouvillain, and P. Camy, "Watt-level diode-pumped
1136 thulium lasers around 2.3 μm ," *Appl. Opt.* **59**, 7530–7539 (2020).
- 1137 61. Z. Pan, Y. Wang, Y. Zhao, H. Yuan, X. Dai, H. Cai, J. E. Bae, S. Y. Choi,
1138 F. Rotermund, X. Mateos, J. M. Serres, P. Loiko, U. Griebner, and V.
1139 Petrov, "Generation of 84-fs pulses from a mode-locked $\text{Tm}:\text{CNNGG}$
1140 disordered garnet crystal laser," *Photon. Res.* **6**, 800–804 (2018).
- 1141 62. Y. Wang, W. Chen, M. Mero, L. Zhang, H. Lin, Z. Lin, G. Zhang,
1142 F. Rotermund, Y. J. Cho, P. Loiko, X. Mateos, U. Griebner, and V.
1143 Petrov, "Sub-100 fs $\text{Tm}:\text{MgWO}_4$ laser at 2017 nm mode locked by a
1144 graphene saturable absorber," *Opt. Lett.* **42**, 3076–3079 (2017).
- 1145 1146

- 1147
1148
1149
1150
1151
63. P. Loiko, R. Thouroude, R. Soulard, L. Guillemot, G. Brasse, B. Guichardaz, A. Braud, A. Hideur, M. Laroche, H. Gilles, and P. Camy, "In-band pumping of Tm:LiYF₄ channel waveguide: a power scaling strategy for ~2 μm waveguide lasers," *Opt. Lett.* **44**, 3010–3013 (2019).
64. A. Tyazhev, F. Starecki, S. Cozic, P. Loiko, L. Guillemot, A. Braud, F. Joulain, M. Tang, T. Godin, A. Hideur, and P. Camy, "Watt-level efficient 2.3 μm thulium fluoride fiber laser," *Opt. Lett.* **45**, 5788–5791 (2020).
- 1152
1153
1154
1155